8 SCIENTIFIC HIGHLIGHT OF THE MONTH

The SIESTA method for linear scaling ab initio simulations

J. M. Soler,[1] E. Artacho,[2] J. D. Gale,[3] A. García,[4]
J. Junquera,[1,5] D. Sánchez-Portal[6] and P. Ordejón[7]

[1] Depto. de Física de Materia Condensada (C-III), Univ. Autónoma de Madrid, 28049 Madrid, Spain
[2] Dept. of Earth Sciences, University of Cambridge, Downing St., Cambridge CB2 3EQ, U. K.
[3] Dept. of Chemistry, Imperial College, South Kensington SW7 2AY, U. K.
[4] Depto. de Física de la Materia Condensada, Univ. del País Vasco, Apt. 644, 48080 Bilbao, Spain
[5] Institut de Physique, Bâtiment B5, Université de Liège, B-4000 Sart-Tilman, Belgium
[6] Dept. de Física de Materiales and DIPC, Univ. del País Vasco, Apt. 1072, 20080 Donostia, Spain
[7] Institut de Ciència de Materials de Barcelona, CSIC, Campus de la UAB, 08193 Bellaterra, Spain

Abstract

We present SIESTA, a self-consistent density functional method using standard norm-conserving pseudopotentials and a flexible, numerical LCAO basis set, which includes multiple-zeta and polarization orbitals. Exchange and correlation are treated with the local spin density or generalized gradient approximations. The basis functions and the electron density are projected on a real-space grid, where the Hartree and exchange-correlation potentials and matrix elements are calculatd with a number of operations that scales linearly with the size of the system. We use a modified energy functional, whose minimization produces orthogonal wavefunctions and the same energy and density as the Kohn-Sham energy functional, without the need of an explicit orthogonalization. Additionally, using localized Wannier-like electron wavefunctions allows the computation time and memory, required to minimize the energy, to also scale linearly with the size of the system. Forces and stresses are also calculated efficiently and accurately, thus allowing structural relaxation and molecular dynamics simulations.

1. Introduction

The improvements in computer hardware and software is allowing the simulation of molecules and materials with an increasing number of atoms N, thus making the use of so-called order-N algorithms (in which the computer time and memory scales linearly with the simulated system size) increasingly important. Although these $\mathcal{O}(N)$ methods were available for classical potentials (including long range interactions) since the 1970's and 80's [1, 2], only in the last 5-10 years have they been developed for the much more complex quantum-mechanical methods. In these, linear scaling algorithms were first implemented in the most simple context of empirical or semiempirical tight-binding methods [3, 4] and in 'ab-initio' nonorthogonal-tight-binding and nonself-consistent Harris-functional methods [5, 6]. However, fully self-consistent density functional theory (DFT) methods [7], more reliable but also considerably more complex, pose the additional problem of the determination of the self-consistent Hamiltonian in $\mathcal{O}(N)$ iterations [8]. While this is difficult using plane waves, a localized basis set appears to be the natural choice. One proposed approach are the 'blips' of Hernandez and Gillan [9], regularly-spaced Gaussian-like splines that can be systematically increased, in the spirit of finite-element methods, although at a considerable computational cost.

We have developed a fully self-consistent DFT scheme, based on flexible linear combination of atomic orbitals (LCAO) basis sets, with essentially perfect $\mathcal{O}(N)$ scaling. It allows extremely fast simulations using minimal basis sets and very accurate calculations with complete multiple-ζ and polarized bases, depending on the required accuracy and available computational power. Apart from that of Born and Oppenheimer, the most basic approximations concern the treatment of exchange and correlation, and the use of pseudopotentials. Exchange and correlation (XC) are treated within Kohn-Sham DFT [10], with either the local (spin) density approximation [11] (LDA/LSD) or the generalized gradient approximation [12] (GGA). We use standard norm-conserving pseudopotentials [13, 14] in their fully non-local form [15], including scalar-relativistic effects and nonlinear partial-core-corrections for XC in the core region [16].

In previous papers [17, 18] we have described preliminary versions of this method, that we call SIESTA (Spanish Initiative for Electronic Simulations with Thousands of Atoms). There is also a review [19] of the tens of studies in a wide variety of systems, like metallic surfaces, nanotubes, and biomolecules, and for a large number of properties. Here we present a more complete description of the method, and illustrate the convergence of a few characteristic magnitudes with respect to the main precision parameters that characterize our method: basis size (number of atomic basis orbitals); basis range (radius of the basis orbitals); fineness of the real-space integration grid; and confinement radius of the Wannier-like electron states. We also show comparisons of results obtained with SIESTA with those of other *ab-initio* approaches to show the quality of the method. In particular, we will focus on the structure of molecular systems, including H-bonding in DNA base-pairs, and on the ferroelectric distortion in cubic $BaTiO_3$.

2. Pseudopotentials

We use first principles norm-conserving pseudopotentials [13] to elliminate the core electrons and, more importantly, to allow for the expansion of a smooth (pseudo)charge density on a uniform spatial grid. SIESTA reads them in semilocal form (a different radial potential $V_l(r)$ for each angular momentum l, optionally generated scalar-relativistically [20, 21]) from a data file that users can fill with their preferred choice. We generally use the Troullier-Martins parameterization [22]. We transform this semilocal form into the fully non-local form proposed by Kleinman and Bylander (KB) [15]:

$$\hat{V}^{PS} = V_{local}(r) + \hat{V}^{KB} \tag{3}$$

$$\hat{V}^{KB} = \sum_{l=0}^{l_{max}^{KB}} \sum_{m=-l}^{l} \sum_{n=1}^{N_l^{KB}} |\chi_{lmn}^{KB}\rangle v_{ln}^{KB} \langle\chi_{lmn}^{KB}| \tag{4}$$

$$v_{ln}^{KB} =< \varphi_{ln}|\delta V_l(r)|\varphi_{ln} > \tag{5}$$

where $\delta V_l(r) = V_l(r) - V_{local}(r)$. $\chi_{lmn}^{KB}(\mathbf{r}) = \chi_{ln}^{KB}(r) Y_{lm}(\hat{\mathbf{r}})$ (with $Y_{lm}(\hat{\mathbf{r}})$ a spherical harmonic) are the KB projection functions

$$\chi_{ln}^{KB}(r) = \delta V_l(r) \varphi_{ln}(r). \tag{6}$$

The functions φ_{ln} are obtained from the eigenstates ψ_{ln} of the semilocal pseudopotential (screened by the pseudo-valence charge density) at energy ϵ_{ln} using the orthogonalization scheme proposed by Blöchl [23]:

$$\varphi_{ln}(r) = \psi_{ln}(r) - \sum_{n'=1}^{n-1} \varphi_{ln'}(r) \frac{< \varphi_{ln'}|\delta V_l(r)|\psi_{ln} >}{< \varphi_{ln'}|\delta V_l(r)|\varphi_{ln'} >} \tag{7}$$

$$\left[-\frac{1}{2r}\frac{d^2}{dr^2} r + \frac{l(l+1)}{2r^2} + V_l(r) + + V^H(r) + V^{xc}(r) \right] \psi_{ln}(r) = \epsilon_{ln} \psi_{ln}(r) \tag{8}$$

V^H and V^{xc} are the Hartree and XC potentials for the pseudo-valence charge density, and we are using atomic units ($e = \hbar = m_e = 1$) throughout this work.

The local part of the pseudopotential $V_{local}(r)$ is in principle arbitrary, but it must join the semilocal potentials $V_l(r)$ which, by construction, all become equal to the (unscreened) all-electron potential beyond the pseudopotential core radius r_{core}. Thus, $\delta V_l(r) = 0$ for $r > r_{core}$. Ramer and Rappe have proposed that $V_{local}(r)$ be optimized for transferability [24], but most plane wave schemes make it equal to one of the $V_l(r)$'s for reasons of efficiency. Our case is different because $V_{local}(r)$ is the only pseudopotential part that needs to be represented in the real space grid, while the matrix elements of the non-local part $\hat{V}_{KB}$ are cheaply and accurately calculated by two-center integrals. Therefore, we optimize $V_{local}(r)$ for smoothness, making it equal to the potential created by a positive charge distribution of the form [25]

$$\rho^{local}(r) \propto \exp[-(\sinh(abr)/\sinh(b))^2], \tag{9}$$

where a and b are chosen to provide simultaneously optimal real-space localization and reciprocal-space convergence [26]. After some numerical tests we have taken b =1 and a =1.82/r_{core}. Figure 2 shows $V_{local}(r)$ for silicon.

Since $V_l(r) = V_{local}(r)$ outside r_{core}, $\chi_{ln}^{KB}(r)$ is strictly zero beyond that radius, irrespective of the value of ϵ_{ln}. Generally it is sufficient to have a single projector χ_{lm}^{KB} for each angular momentum (i.e. a single term in the sum on n). In this case we follow the normal practice of making ϵ_{ln} equal to the valence atomic eigenvalue ϵ_l, and the function $\varphi_l(r)$ in Eq. 6 is identical to the corresponding eigenstate $\psi_l(r)$. In some cases, particularly for alkaline metals, alkaline earths, and transition metals of the first few columns, we have sometimes found it necessary to include the semicore states together with the valence states [27]. In these cases, we also include two independent KB projectors, one for the semicore and one for the valence states. Also, since the non-local part of the pseudopotential is a relatively cheap operator within SIESTA, we generally (but not necessarily) use a larger than usual value of l_{max}^{KB} in Eq. (4), making it one unit larger than the l_{max} of the basis functions.

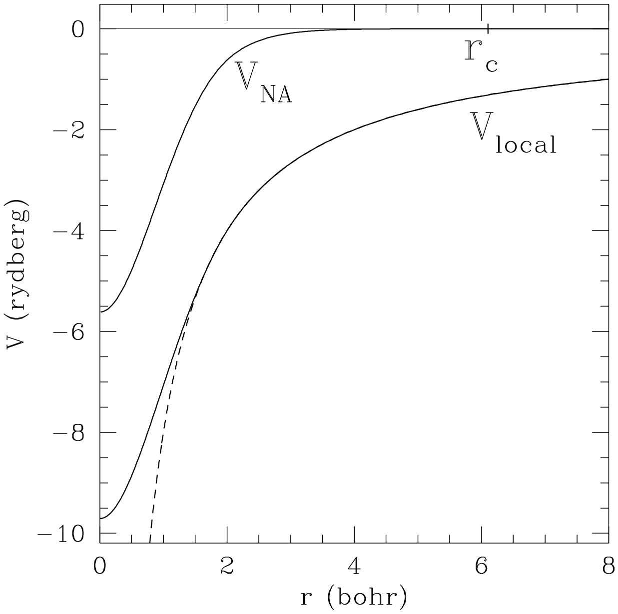

Figure 2: Local pseudopotential for silicon. V_{local} is the unscreened local part of the pseudopotential, generated as the electrostatic potential produced by a localized distribution of positive charge, Eq. (9), whose integral is equal to the valence ion charge ($Z = 4$ for Si). The dashed line is $-Z/r$. V_{NA} is the local pseudopotential screened by an electron charge distribution, generated by filling the first-ζ basis orbitals with the free-atom valence occupations. Since these basis orbitals are strictly confined to a radius r_{max}^c, V_{NA} is also strictly zero beyond that radius.

3. Basis set

Order-N methods rely heavily on the sparsity of the Hamiltonian and overlap matrices. This sparsity requires either the neglect of matrix elements that are small enough or the use of strictly confined basis orbitals, *i.e.*, orbitals that are zero beyond a certain radius [6]. We have adopted this latter approach because it keeps the energy strictly variational, thus facilitating the test of the convergence with respect to the radius of confinement. Within this radius, our atomic basis orbitals are products of a numerical radial function times a spherical harmonic. For atom I, located at $\mathbf{R}_I$,

$$\phi_{Ilmn}(\mathbf{r}) = \phi_{Iln}(r_I)Y_{lm}(\hat{\mathbf{r}}_I) \tag{10}$$

where $\mathbf{r}_I = \mathbf{r} - \mathbf{R}_I$, $r = |\mathbf{r}|$ and $\hat{\mathbf{r}} = \mathbf{r}/r$. The angular momentum (labelled by l, m) may be arbitrarily large and, in general, there will be several orbitals (labelled by index n) with the same angular dependence, but different radial dependence, which is conventionally called a 'multiple-ζ' basis. The radial functions are defined by a cubic spline interpolation [28] from the values given on a fine radial mesh. Each radial function may have a different cutoff radius and, up to that radius, its shape is completely free and can be introduced by the user in an input file. In practice, it is also convenient to have an automatic procedure to generate sufficiently good basis sets. We have developed several such automatic procedures, and we will describe here one of them for completeness, even though we stress that the generation of the basis set, like that of the pseudopotential is to a large extent up to the user and independent of the SIESTA method itself.

In the case of a minimal (single-ζ) basis set, we have found convenient and efficient the method of Sankey and Niklewski [6, 29]. Their basis orbitals are the eigenfunctions of the (pseudo)atom within a spherical box (although the radius of the box may be different for each orbital, see below). In other words, they are the (angular-momentum-dependent) numerical eigenfunctions $\phi_l(r)$ of the atomic pseudopotential $V_l(r)$, for an energy $\epsilon_l + \delta\epsilon_l$ chosen so that the first node occurs at the desired cutoff radius r_l^c:

$$\left(-\frac{1}{2r}\frac{d^2}{dr^2}r + \frac{l(l+1)}{2r^2} + V_l(r) \right) \phi_l(r) = (\epsilon_l + \delta\epsilon_l)\phi_l(r) \tag{11}$$

with $\phi_l(r_l^c) = 0$ (we omit indices I and n here for simplicity). In order to obtain a well balanced basis, in which the effect of the confinement is similar for all the orbitals, it is usually better to fix a common 'energy shift' $\delta\epsilon$, rather than a common radius r^c, for all the atoms and angular momenta. This means that the orbital radii depend on the atomic species and angular momentum.

One obvious possibility for multiple-ζ bases is to use pseudopotential eigenfunctions with an increasing number of nodes [29]. They have the virtue of being orthogonal and asymptotically complete. However, the efficiency of this kind of basis depends on the radii of confinement of the different orbitals, since the excited states of the pseudopotential are usually unbound. Thus, in practice we have found this procedure rather inefficient. Another possibility is to use the atomic eigenstates for different ionization states [30]. We have implemented a different scheme [31], based on the 'split-valence' method which is standard in quantum chemistry [32]. In that method, the first-ζ basis orbitals are 'contracted' (i.e. fixed) linear combinations of Gaussians, determined either variationally or by fitting numerical atomic eigenfunctions. The second-ζ orbital is then one of the Gaussians (generally the slowest-decaying one) which is 'released' or 'split' from the contracted combination. Higher-ζ orbitals are generated in a similar way by releasing more Gaussians. Our scheme adapts this split-valence method to our numerical orbitals. Following the same spirit, our second-ζ functions $\phi_l^{2\zeta}(r)$ have the same tail as the first-ζ orbitals $\phi_l^{1\zeta}(r)$ but change to a simple polynomial behaviour inside a 'split radius' r_l^s:

$$\phi_l^{2\zeta}(r) = \begin{cases} r^l(a_l - b_l r^2) & \text{if } r < r_l^s \\ \phi_l^{1\zeta}(r) & \text{if } r \geq r_l^s \end{cases} \tag{12}$$

where a_l and b_l are determined by imposing the continuity of value and slope at r_l^s. These orbitals therefore combine the decay of the atomic eigenfunctions with a smooth and featureless behaviour inside r_l^s. We have found it convenient to set the radius r_l^s by fixing the norm of $\phi_l^{1\zeta}$ in $r > r_l^s$; in practice, a reasonable value for this 'split-norm' is ~ 0.15. Actually, instead of $\phi_l^{2\zeta}$ thus defined, we use $\phi_l^{1\zeta} - \phi_l^{2\zeta}$, which is zero beyond r_l^s, to reduce the number of nonzero matrix elements, without any loss of variational freedom.

To achieve well converged results, in addition to the atomic valence orbitals, it is generally necessary to also include polarization orbitals, to account for the deformation induced by bond formation. Again, using pseudoatomic orbitals of higher angular momentum is frequently unsatisfactory, because they tend to be too extended, or even unbound. Instead, consider a valence pseudoatomic orbital $\phi_{lm}(\mathbf{r}) = \phi_l(r)Y_{lm}(\hat{\mathbf{r}})$, such that there are no valence orbitals with angular momentum $l+1$. To polarize it, we apply a small electric field $\mathcal{E}$ in the z-direction, and use first-order perturbation theory. Selection rules imply that the resulting perturbed orbital will only have components with $l' = l \pm 1, m' = m$. Since in general there will already be orbitals with angular momentum $l-1$ in the basis set, we select only the $l+1$ component. Thus we obtain the equation

$$\left[-\frac{1}{2r}\frac{d^2}{dr^2}r + \frac{(l+1)(l+2)}{2r^2} + V_l(r) - E_l \right] \varphi_{l+1}(r) = -r\phi_l(r) \tag{13}$$

which defines the polarization orbitals that are then added to the basis set: $\phi_{l+1,m}(\mathbf{r}) = C\varphi_{l+1}(r)Y_{l+1,m}(\hat{\mathbf{r}})$, where C is a normalization constant.

We have found that the previously described procedures generate reasonable minimal single-ζ (SZ) basis sets, appropriate for semiquantitative simulations, and double-ζ plus polarization (DZP) basis sets that yield high quality results for most of the systems studied. We thus refer to DZP as the 'standard' basis, because it usually represents a good balance between well converged results and a reasonable computational cost. In some cases (typically alkali and some transition metals), semicore states also need to be included for good quality results. More recently [33], we have obtained extremely efficient basis sets optimized variationally in molecules or solids. Figure 3 shows the performance of these atomic basis sets compared to plane waves, using the same pseudopotentials and geometries. It may be seen that the SZ bases are comparable to planewave cutoffs typically used in Car-Parrinello molecular dynamics simulations, while DZP sets are comparable to the cutoffs used in geometry relaxations and energy comparisons. As expected, the LCAO is far more efficient, tipically by a factor of 10 to 20, in terms of number of basis orbitals. This efficiency must be balanced against the faster algorithms available for plane waves, and our main motivation for using an LCAO basis is its suitability for $\mathcal{O}(N)$ methods. Still, we have generally found that, even without using the $\mathcal{O}(N)$ functional, Siesta is considerably faster than a plane wave calculation of similar quality.

Table 2 shows the convergence of the lattice constant, bulk modulus and cohesive energy for silicon for different basis sets, and the correponding values for plane waves and LAPW calculations and the experiment. It can be seen that the 'standard' DZP basis offers already quite well converged results, comparable to those used in practice in most plane wave calculations.

Figure 4 shows the dependence of the lattice constant, bulk modulus, and cohesive energy of bulk silicon with the range of the basis orbitals, showing that a cutoff radius of 3 Å for both s and p orbitals yields very well converged results, specially when using a 'standard' DZP basis.

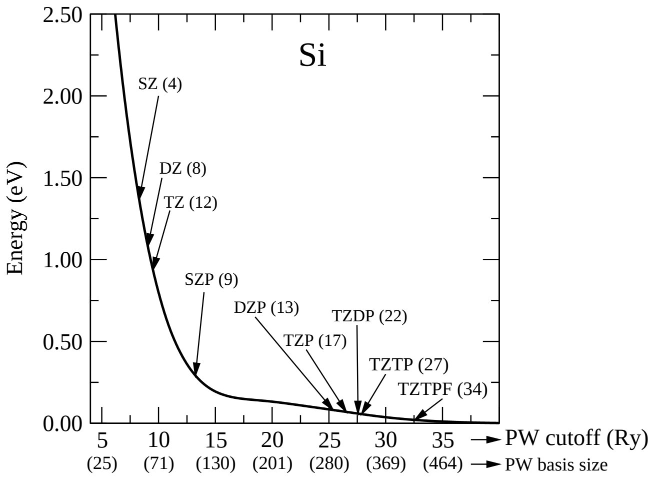

Figure 3: Comparison of convergence of the total energy with respect to the sizes of a plane wave basis set and of the LCAO basis set used by Siesta. The curve shows the total energy per atom of silicon versus the cutoff of a plane wave basis, calculated with a program independent of Siesta, which uses the same pseudopotential. The arrows indicate the energies obtained with different LCAO basis sets, calculated with Siesta, and the plane wave cutoffs that yield the same energies. The numbers in parentheses indicate the basis sizes, i.e. the number of atomic orbitals or plane waves of each basis set. SZ: single-ζ (valence s and p orbitals); DZ: double-ζ; TZ: triple-ζ; DZP: double-ζ valence orbitals plus single-ζ polarization d orbitals; TZP: triple-ζ valence plus single-ζ polarization; TZDP: triple-ζ valence plus double-ζ polarization; TZTP: triple-ζ valence plus triple-ζ polarization; TZTPF: same as TZTP plus extra single-ζ polarization f orbitals.

Table 2: Comparisons of the lattice constant a, bulk modulus B, and cohesive energy E_c for bulk Si, obtained with different basis sets. The basis notation is as in Fig. 3. PW refers to a 50 Ry-cutoff plane wave calculation. The LAPW results were taken from ref. [34], and the experimental values from ref. [35].

Basis	a (Å)	B (GPa)	E_c (eV)
SZ	5.521	88.7	4.722
DZ	5.465	96.0	4.841
TZ	5.453	98.4	4.908
SZP	5.424	97.8	5.227
DZP	5.389	96.6	5.329
TZP	5.387	97.5	5.335
TZDP	5.389	96.0	5.340
TZTP	5.387	96.0	5.342
TZTPF	5.385	95.4	5.359
PW	5.384	95.9	5.369
LAPW	5.41	96	5.28
Expt.	5.43	98.8	4.63

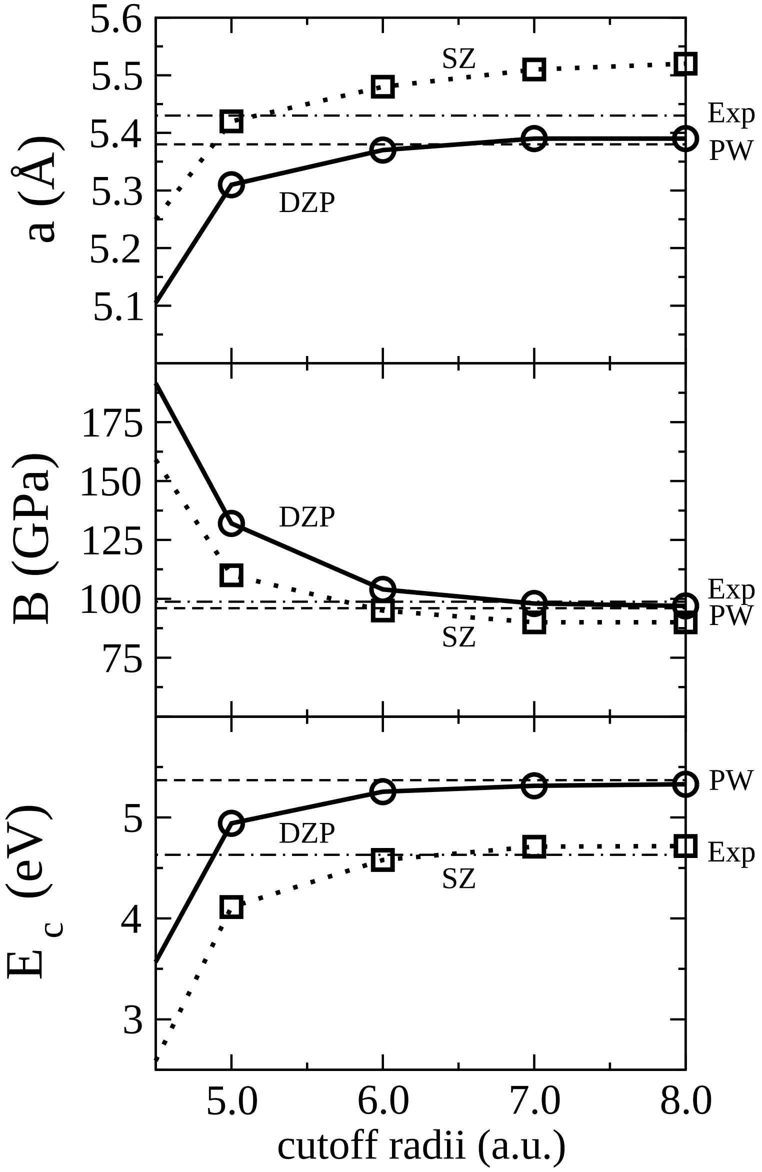

Figure 4: Dependence of the lattice constant, bulk modulus, and cohesive energy of bulk silicon with the cutoff radius of the basis orbitals. The s and p orbital radii have been made equal in this case, to simplify the plot. PW refers to a well converged plane wave calculation with the same pseudopotential.

4. Electron Hamiltonian

Within the non-local-pseudopotential approximation, the standard Kohn-Sham one-electron Hamiltonian may be written as

$$\hat{H} = \hat{T} + \sum_I V_I^{local}(\mathbf{r}) + \sum_I \hat{V}_I^{KB} + V^H(\mathbf{r}) + V^{xc}(\mathbf{r}) \tag{14}$$

where $\hat{T} = -\frac{1}{2}\nabla^2$ is the kinetic energy operator, I is an atom index, $V^H(\mathbf{r})$ and $V^{xc}(\mathbf{r})$ are the total Hartree and XC potentials, and $V_I^{local}(\mathbf{r})$ and $\hat{V}_I^{KB}$ are the local and non-local (Kleinman-Bylander) parts of the pseudopotential of atom I.

In order to eliminate the long range of V_I^{local}, we screen it with the potential V_I^{atom}, created by an atomic electron density ρ_I^{atom}, constructed by populating the basis functions with appropriate valence atomic charges. Notice that, since the atomic basis orbitals are zero beyond the cutoff radius $r_I^c = \max_l(r_{Il}^c)$, the screened 'neutral-atom' (NA) potential $V_I^{NA} \equiv V_I^{local} + V_I^{atom}$ is also zero beyond this radius [6] (see Fig. 2). Now let $\delta\rho(\mathbf{r})$ be the difference between the self-consistent electron density $\rho(\mathbf{r})$ and the sum of atomic densities $\rho^{atom} = \sum_I \rho_I^{atom}$, and let $\delta V^H(\mathbf{r})$ be the electrostatic potential generated by $\delta\rho(\mathbf{r})$, which integrates to zero and is usually much smaller than $\rho(\mathbf{r})$. Then the total Hamiltonian may be rewritten as

$$\hat{H} = \hat{T} + \sum_I \hat{V}_I^{KB} + \sum_I V_I^{NA}(\mathbf{r}) + \delta V^H(\mathbf{r}) + V^{xc}(\mathbf{r}) \tag{15}$$

The matrix elements of the first two terms involve only two-center integrals which are calculated in reciprocal space and tabulated as a function of interatomic distance. The remaining terms involve potentials which are calculated on a three-dimensional real-space grid. We consider these two approaches in detail in the following sections.

5. Two-center integrals

The overlap matrix and the largest part of the Hamiltonian matrix elements are given by two-center integrals [36]. We calculate these integrals in Fourier space, as proposed by Sankey and Niklewski [6], but we use some implementation details explained in this section. Let us consider first overlap integrals of the form

$$S(\mathbf{R}) \equiv \langle \psi_1 | \psi_2 \rangle = \int \psi_1^*(\mathbf{r})\psi_2(\mathbf{r} - \mathbf{R}) d\mathbf{r}, \tag{16}$$

where the integral is over all space and ψ_1, ψ_2 may be basis functions ϕ_{lmn}, KB pseudopotential projectors χ_{lmn}, or more complicated functions centered on the atoms. The function $S(\mathbf{R})$ can be seen as a convolution: we take the Fourier transform

$$\psi(\mathbf{k}) = \frac{1}{(2\pi)^{3/2}} \int \psi(\mathbf{r}) e^{-i\mathbf{kr}} d\mathbf{r} \tag{17}$$

Using the planewave expression of Dirac's delta function, $\int e^{i(\mathbf{k}'-\mathbf{k})\mathbf{r}} d\mathbf{r} = (2\pi)^3 \delta(\mathbf{k}' - \mathbf{k})$, we find the usual result that the Fourier transform of a convolution in real space is a simple product in reciprocal space:

$$S(\mathbf{R}) = \int \psi_1^*(\mathbf{k})\psi_2(\mathbf{k}) e^{-i\mathbf{kR}} d\mathbf{k} \tag{18}$$

Let us assume now that the functions $\psi(\mathbf{r})$ can be expanded exactly with a finite number of spherical harmonics:

$$\psi(\mathbf{r}) = \sum_{l=0}^{l_{max}} \sum_{m=-l}^{l} \psi_{lm}(r) Y_{lm}(\hat{\mathbf{r}}), \tag{19}$$

$$\psi_{lm}(r) = \int_0^{\pi} \sin\theta d\theta \int_0^{2\pi} d\varphi Y_{lm}^*(\theta,\varphi)\psi(r,\theta,\varphi). \tag{20}$$

This is clearly true for basis functions and KB projectors, which contain a single spherical harmonic, and also for functions like $x\psi(\mathbf{r})$, which appear in dipole matrix elements. We now substitute in (17) the expansion of a plane wave in spherical harmonics [37]

$$e^{i\mathbf{kr}} = \sum_{l=0}^{\infty} \sum_{m=-l}^{l} 4\pi i^l j_l(kr) Y_{lm}^*(\hat{\mathbf{k}}) Y_{lm}(\hat{\mathbf{r}}), \tag{21}$$

to obtain

$$\psi(\mathbf{k}) = \sum_{l=0}^{l_{max}} \sum_{m=-l}^{l} \psi_{lm}(k) Y_{lm}(\hat{\mathbf{k}}), \tag{22}$$

$$\psi_{lm}(k) = \sqrt{\frac{2}{\pi}}(-i)^l \int_0^{\infty} r^2 dr j_l(kr)\psi_{lm}(r). \tag{23}$$

Substituting now (22) and (21) into (18) we obtain

$$S(\mathbf{R}) = \sum_{l=0}^{2l_{max}} \sum_{m=-l}^{l} S_{lm}(R) Y_{lm}(\hat{\mathbf{R}}) \tag{24}$$

where

$$S_{lm}(R) = \sum_{l_1 m_1} \sum_{l_2 m_2} G_{l_1 m_1, l_2 m_2, lm} S_{l_1 m_1, l_2 m_2, l}(R), \tag{25}$$

$$G_{l_1 m_1, l_2 m_2, lm} = \int_0^{\pi} \sin\theta d\theta \int_0^{2\pi} d\varphi Y_{l_1 m_1}^*(\theta,\varphi) Y_{l_2 m_2}(\theta,\varphi) Y_{lm}^*(\theta,\varphi), \tag{26}$$

$$S_{l_1 m_1, l_2 m_2, l}(R) = 4\pi i^{l_1 - l_2 - l} \int_0^{\infty} k^2 dk j_l(kR) i^{-l_1} \psi_{1,l_1 m_1}^*(k) i^{l_2} \psi_{2,l_2 m_2}(k), \tag{27}$$

Notice that $i^{-l_1}\psi_1(k), i^{l_2}\psi_2(k)$, and $i^{l_1-l_2-l}$ are all real, since $l_1 - l_2 - l$ is even for all l's for which $G_{l_1 m_1, l_2 m_2, lm} \neq 0$. The Gaunt coefficients $G_{l_1 m_1, l_2 m_2, lm}$ can be obtained by recursion from Clebsch-Gordan coefficients [6]. However, we use real spherical harmonics for computational efficiency:

$$Y_{lm}(\theta,\varphi) = C_{lm} P_l^m(\cos\theta) \times \begin{cases} \sin(m\varphi) & \text{if } m < 0 \\ \cos(m\varphi) & \text{if } m \geq 0 \end{cases} \tag{28}$$

where $P_l^m(z)$ are the associated Legendre polynomials and C_{lm} normalization constants [28]. This does not affect the validity of any of previous equations, but it modifies the value of the Gaunt coefficients. Therefore, we find it is simpler and more general to calculate $G_{l_1 m_1, l_2 m_2, lm}$ directly from Eq. (26). To do this, we use a Gaussian quadrature [28]

$$\int_0^{\pi} \sin\theta d\theta \int_0^{2\pi} d\varphi \to 4\pi \frac{1}{N_\theta} \sum_{i=1}^{N_\theta} w_i \sin\theta_i \frac{1}{N_\varphi} \sum_{j=1}^{N_\varphi} \tag{29}$$

with $N_\varphi = 1 + 3l_{max}, N_\theta = 1 + \mathrm{int}(3l_{max}/2)$, and the points $\cos\theta_i$ and weights w_i are calculated as described in ref. [28]. This quadrature is exact in equation (26) for spherical harmonics Y_{lm}

(real or complex) of $l \leq l_{max}$, and it can be used also to find the expansion of $\psi(\mathbf{r})$ in spherical harmonics (eq. (20)).

The coefficients $G_{l_1m_1,l_2m_2,lm}$ are universal and they can be calculated and stored once and for all. The functions $S_{l_1m_1,l_2m_2,l}(R)$ depend, of course, on the functions $\psi_{1,2}(\mathbf{r})$ being integrated. For each pair of functions, they can be calculated and stored in a fine radial grid R_i, up to the maximum distance $R_{max} = r_1^c + r_2^c$ at which ψ_1 and ψ_2 overlap. Their value at an arbitrary distance R can then be obtained very accurately using a spline interpolation.

Kinetic matrix elements $T(\mathbf{R}) \equiv \langle \psi_1^* | -\frac{1}{2}\nabla^2 | \psi_2 \rangle$ can be obtained in exactly the same way, except for an extra factor k^2 in Eq. (27):

$$T_{l_1m,l_2m_2,l}(R) = 4\pi i^{l_1-l_2-l} \int_0^\infty \frac{1}{2} k^4 dk j_l(kR) i^{-l_1} \psi_{1,l_1m_1}^*(k) i^{l_2} \psi_{2,l_2m_2}(k). \tag{30}$$

Since we frequently use basis orbitals with a kink [6], we need rather fine radial grids to obtain accurate kinetic matrix elements, and we typically use grid cutoffs of more than 2000 Ry for this purpose. Once obtained, the fine grid does not penalize the execution time, because the interpolation effort is independent of the number of grid points. It also affects very marginally the storage requirements, because of the one-dimensional character of the tables. However, even though it needs to be done only once, the calculation of the radial integrals (23), (27), and (30) is not negligible if performed unwisely. We have developed a special fast radial Fourier transform for this purpose, as explained elsewhere [38]

Dipole matrix elements, such as $\langle \psi_1 | x | \psi_2 \rangle$, can also be obtained easily by defining a new function $\chi_1(\mathbf{r}) \equiv x\psi_1(\mathbf{r})$, expanding it using (20), and computing $\langle \chi_1 | \psi_2 \rangle$ as explained above (with the precaution of using $l_{max} + 1$ instead of l_{max}).

6. Grid integrals

The matrix elements of the last three terms of Eq. (15) involve potentials which are calculated on a real-space grid. The fineness of this grid is controlled by a 'grid cutoff' E_{cut}: the maximum kinetic energy of the planewaves that can be represented in the grid without aliasing [39]. The short-range screened pseudopotentials $V_I^{NA}(\mathbf{r})$ in (15) are tabulated as a function of the distance to atoms I and easily interpolated at any desired grid point. The last two terms require the calculation of the electron density on the grid. Let $\psi_i(\mathbf{r})$ be the Hamiltonian eigenstates, expanded in the atomic basis set

$$\psi_i(\mathbf{r}) = \sum_\mu \phi_\mu(\mathbf{r}) c_{\mu i}, \tag{31}$$

where $c_{\mu i} = \langle \tilde{\phi}_\mu | \psi_i \rangle$ and $\tilde{\phi}_\mu$ is the dual orbital of ϕ_μ: $\langle \tilde{\phi}_\mu | \phi_\nu \rangle = \delta_{\mu\nu}$. We use the compact index notation $\mu \equiv \{Ilmn\}$ for the basis orbitals, Eq. (10). The electron density is then

$$\rho(\mathbf{r}) = \sum_i n_i |\psi_i(\mathbf{r})|^2 \tag{32}$$

where n_i is the occupation of state ψ_i. If we substitute (31) into (32) and define a density matrix

$$\rho_{\mu\nu} = \sum_i c_{\mu i} n_i c_{i\nu}, \tag{33}$$

where $c_{i\nu} \equiv c^*_{\nu i}$, the electron density can be rewritten as

$$\rho(\mathbf{r}) = \sum_{\mu\nu} \rho_{\mu\nu} \phi^*_\nu(\mathbf{r}) \phi_\mu(\mathbf{r}) \tag{34}$$

To calculate the density at a given grid point, we first find all the atomic basis orbitals, Eq. (10), at that point, interpolating the radial part from numerical tables, and then use (34) to calculate the density. Notice that only a small number of basis orbitals are non-zero at a given grid point, so that the calculation of the density can be performed in $\mathcal{O}(N)$ operations, once $\rho_{\mu\nu}$ is known. The calculation of $\rho_{\mu\nu}$ itself with Eq. (33) does not scale linearly with the system size, requiring instead the use of special $\mathcal{O}(N)$ techniques to be described below. However, notice that in order to calculate the density, only the matrix elements $\rho_{\mu\nu}$ for which ϕ_μ and ϕ_ν overlap are required, and they can therefore be stored as a sparse matrix of $\mathcal{O}(N)$ size. Once the valence density is available in the grid, we add to it, if necessary, the non-local core correction [16], a spherical charge density intended to simulate the atomic cores, which is also interpolated from a radial grid. With it, we find the exchange and correlation potential $V^{xc}(\mathbf{r})$, trivially in the LDA and using the method described in ref. [40] for the GGA. To calculate $\delta V^H(\mathbf{r})$, we first find $\rho^{atom}(\mathbf{r})$ at the grid points, as a sum of spherical atomic densities (also interpolated from a radial grid) and subtract it from $\rho(\mathbf{r})$ to find $\delta\rho(\mathbf{r})$. We then solve Poisson's equation to obtain $\delta V^H(\mathbf{r})$ and find the total grid potential $V(\mathbf{r}) = V^{NA}(\mathbf{r}) + \delta V^H(\mathbf{r}) + V^{xc}(\mathbf{r})$. Finally, at every grid point, we calculate $V(\mathbf{r})\phi^*_\mu(\mathbf{r})\phi_\nu(\mathbf{r})\Delta\mathbf{r}^3$ for all pairs ϕ_μ, ϕ_ν which are not zero at that point ($\Delta\mathbf{r}^3$ is the volume per grid point) and add it to the Hamiltonian matrix element $H_{\mu\nu}$.

To solve Poisson's equation and find $\delta V^H(\mathbf{r})$ we normally use fast Fourier transforms in a unit cell that is either naturally periodic or made artificially periodic by a supercell construction. For neutral isolated molecules, our use of strictly confined basis orbitals makes it trivial to avoid any direct overlap between the repeated molecules, and the electric multipole interactions decrease rapidly with cell size. For charged molecules we supress the $\mathbf{G} = 0$ Fourier component (an infinite constant) of the potential created by the excess of charge. This amounts to compensating this excess with a uniform charge background. We then use the method of Makov and Payne [41] to correct the total energy for the interaction between the repeated cells. Alternatively, we can solve Poisson's equation by the multigrid method, using finite differences and fixed boundary conditions, obtained from the multipole expansion of the molecular charge density. This can be done in strictly $\mathcal{O}(N)$ operations, unlike the FFT's, which scale as $N \log N$. However, the cost of this operation is typically negligible and therefore has no influence on the overall scaling properties of the calculation.

We have found it convenient for the efficiency of the calculations to use a given grid (defined by E_{cut}) during the self-consistency, and then to refine the integrals using a finer grid in the final calculation of the energy and forces (using the density obtained self-consistently with the original grid). This provides a significant improvement in accuracy with very little computational overhead. The grid refinement is done defining a grid-cell-sampling of several points per each original grid point.

Figure 5 shows the convergence of different magnitudes with respect to the energy cutoff of the integration grid. For orthogonal unit cell vectors this is simply, in atomic units, $E_{cut} = (\pi/\Delta x)^2/2$ with Δx the grid interval.

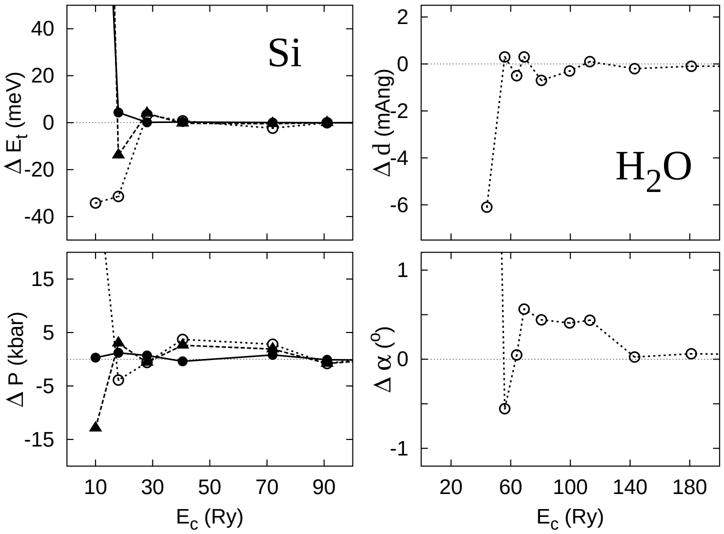

Figure 5: (a) Convergence of the total energy and pressure in bulk silicon as a function of the energy cutoff E_{cut} of the real space integration mesh. Circles and continuous line: using a grid-cell-sampling of eight refinement points per original grid point. The refinement points are used only in the final calculation, not during the self-consistency iteration (see text). Triangles: two refinement points per original grid point. White circles: no grid-cell-sampling. (b) Bond length and angle of the water molecule as a function of E_{cut}

7. Brillouin zone sampling

Integration of all magnitudes over the Brillouin zone (BZ) is essential for small and moderately large unit cells, especially of metals. Although Siesta is designed for large unit cells, in practice it is very useful, especially for comparisons and checks, to be able to also perform calculations efficiently on smaller systems without using expensive superlattices. On the other hand, an efficient k-sampling implementation should not penalize, because of the required complex arithmetic, the Γ-point calculations used in large cells. A solution used in some programs is to have two different versions of all or part of the code, but this poses extra maintenance requirements. We have dealt with this problem in the following way: around the unit cell (and comprising itself) we define an auxiliary supercell large enough to contain all the atoms whose basis orbitals are non-zero at any of the grid points of the unit cell, or which overlap with any of the basis orbitals in it. We calculate all the non-zero two-center integrals between the unit cell basis orbitals and the supercell orbitals, without any complex phase factors. We also calculate the grid integrals between *all* the supercell basis orbitals $\phi_{\mu'}$ and $\phi_{\nu''}$ (primed indices run over all the supercell), but *within the unit cell only.* We accumulate these integrals in the corresponding matrix elements, thus making use of the relation

$$< \phi_\mu | V(\mathbf{r}) | \phi_{\nu'} > = \sum_{(\mu'\nu'') \equiv (\mu\nu')} < \phi_{\mu'} | V(\mathbf{r}) f(\mathbf{r}) | \phi_{\nu''} > . \tag{35}$$

$f(\mathbf{r}) = 1$ for $\mathbf{r}$ within the unit cell and is zero otherwise. ϕ_μ is within the unit cell. The notation $\mu' \equiv \mu$ indicates that $\phi_{\mu'}$ and ϕ_μ are equivalent orbitals, related by a lattice vector translation.

$(\mu'\nu'') \equiv (\mu\nu')$ means that the sum extends over all pairs of supercell orbitals $\phi_{\mu'}$ and $\phi_{\nu''}$ such that $\mu' \equiv \mu$, $\nu'' \equiv \nu'$, and $\mathbf{R}_\mu - \mathbf{R}_{\nu'} = \mathbf{R}_{\mu'} - \mathbf{R}_{\nu''}$. Once all the real overlap and Hamiltonian matrix elements are calculated, we multiply them, at every k-point by the corresponding phase factors and accumulate them by folding the supercell orbital to its unit-cell counterpart. Thus

$$H_{\mu\nu}(\mathbf{k}) = \sum_{\nu' \equiv \nu} H_{\mu\nu'} e^{i\mathbf{k}(\mathbf{R}_{\nu'} - \mathbf{R}_\mu)} \tag{36}$$

where ϕ_μ and ϕ_ν are within the unit cell. The resulting $N \times N$ complex eigenvalue problem, with N the number of orbitals in the unit cell, is then solved at every sampled k point, finding the Bloch-state expansion coefficients $c_{\mu i}(\mathbf{k})$:

$$\psi_i(\mathbf{k}, \mathbf{r}) = \sum_{\mu'} e^{i\mathbf{k}\mathbf{R}_{\mu'}} \phi_{\mu'}(\mathbf{r}) c_{\mu' i}(\mathbf{k}) \tag{37}$$

where the sum in μ' extends to all basis orbitals in space, i labels the different bands, $c_{\mu' i} = c_{\mu i}$ if $\mu' \equiv \mu$, and $\psi_i(\mathbf{k}, \mathbf{r})$ is normalized in the unit cell.

The electron density is then

$$\rho(\mathbf{r}) = \sum_i \int_{BZ} n_i(\mathbf{k}) |\psi_i(\mathbf{k}, \mathbf{r})|^2 d\mathbf{k} = \sum_{\mu'\nu'} \rho_{\mu'\nu'} \phi^*_{\nu'}(\mathbf{r}) \phi_{\mu'}(\mathbf{r}) \tag{38}$$

where the sum is again over all basis orbitals in space, and the density matrix

$$\rho_{\mu\nu} = \sum_i \int_{BZ} c_{\mu i}(\mathbf{k}) n_i(\mathbf{k}) c_{i\nu}(\mathbf{k}) e^{i\mathbf{k}(\mathbf{R}_\nu - \mathbf{R}_\mu)} d\mathbf{k} \tag{39}$$

is real (for real ϕ_μ's) and periodic, i.e. $\rho_{\mu\nu} = \rho_{\mu'\nu'}$ if $(\nu, \mu) \equiv (\nu', \mu')$ (with '$\equiv$' meaning again 'equivalent by translation'). Thus, to calculate the density at a grid point of the unit cell, we simply find the sum (38) over all the pairs of orbitals ϕ_μ, ϕ_ν in the supercell that are non-zero at that point.

In practice, the integral in (39) is performed in a finite, uniform grid of the Brillouin zone. The fineness of this grid is controlled by a k-grid cutoff l_{cut}, a real-space radius which plays a role equivalent to the planewave cutoff of the real-space grid [42]. The origin of the k-grid may be displaced from $\mathbf{k} = 0$ in order to decrease the number of inequivalent k-points [43].

If the unit cell is large enough to allow a Γ-point-only calculation, the multiplication by phase factors is skipped and a single real-matrix eigenvalue problem is solved (in this case, the real matrix elements are accumulated directly in the first stage, if multiple overlaps occur). In this way, no complex arithmetic penalty occurs, and the differences between Γ-point and k-sampling are limited to a very small section of the code, while all the two-center and grid integrals use always the same real-arithmetic code.

8. Total energy

The Kohn-Sham [10] total energy can be written as a sum of a band-structure (BS) energy plus some correction terms, sometimes called 'double count' corrections. The BS term is the sum of the energies of the occupied states ψ_i:

$$E^{BS} = \sum_i n_i \langle \psi_i | \hat{H} | \psi_i \rangle = \sum_{\mu\nu} H_{\mu\nu} \rho_{\nu\mu} = \mathrm{Tr}(H\rho) \tag{40}$$

where spin and k-sampling notations are omitted here for simplicity. At convergence, the ψ_i's are simply the eigenvectors of the Hamiltonian, but it is important to realize that the Kohn-Sham functional is also perfectly well defined outside this so-called 'Born-Oppenheimer surface', i.e. it is defined for any set of orthonormal ψ_i's. The correction terms are simple functionals of the electron density, which can be obtained from equation (34), and the atomic positions. The Kohn-Sham total energy can then be written as

$$E^{KS} = \sum_{\mu\nu} H_{\mu\nu}\rho_{\nu\mu} - \frac{1}{2}\int V^H(\mathbf{r})\rho(\mathbf{r})d^3\mathbf{r} + \int(\epsilon^{xc}(\mathbf{r}) - V^{xc}(\mathbf{r}))\rho(\mathbf{r})d^3\mathbf{r} + \sum_{I<J}\frac{Z_I Z_J}{R_{IJ}} \tag{41}$$

where I, J are atomic indices, $R_{IJ} \equiv |\mathbf{R}_J - \mathbf{R}_I|$, Z_I, Z_J are the valence ion pseudoatom charges, and $\epsilon^{xc}(\mathbf{r})\rho(\mathbf{r})$ is the exchange-correlation energy density. In order to avoid the long range interactions of the last term, we construct from the local-pseudopotential V_I^{local}, which has an asymptotic behavior of $-Z_I/r$, a diffuse ion charge, $\rho_I^{local}(r)$, whose electrostatic potential is equal to $V_I^{local}(r)$:

$$\rho_I^{local}(\mathbf{r}) = -\frac{1}{4\pi}\nabla^2 V_I^{local}(\mathbf{r}). \tag{42}$$

Notice that we define the electron density as positive, and therefore $\rho_I^{local} \leq 0$. Then, we write the last term in (41) as

$$\sum_{I<J}\frac{Z_I Z_J}{R_{IJ}} = \frac{1}{2}\sum_{IJ} U_{IJ}^{local}(R_{IJ}) + \sum_{I<J}\delta U_{IJ}^{local}(R_{IJ}) - \sum_I U_I^{local} \tag{43}$$

where U_{IJ}^{local} is the electrostatic interaction between the diffuse ion charges in atoms I and J:

$$U_{IJ}^{local}(|\mathbf{R}|) = \int V_I^{local}(\mathbf{r})\rho_J^{local}(\mathbf{r}-\mathbf{R})d^3\mathbf{r}, \tag{44}$$

δU_{IJ}^{local} is a small short-range interaction term to correct for a possible overlap between the soft ion charges, which appears when the core densities are very extended:

$$\delta U_{IJ}^{local}(R) = \frac{Z_I Z_J}{R} - U_{IJ}^{local}(R), \tag{45}$$

and U_I^{local} is the fictitious self interaction of an ion charge (notice that the first right-hand sum in (43) includes the $I = J$ terms):

$$U_I^{local} = \frac{1}{2}U_{II}^{local}(0) = \frac{1}{2}\int V_I^{local}(r)\rho_I^{local}(r)4\pi r^2 dr. \tag{46}$$

Defining ρ_I^{NA} from V_I^{NA}, analogously to ρ_I^{local}, we have that $\rho_I^{NA} = \rho_I^{local} + \rho_I^{atom}$, and equation (41) can be transformed, after some rearrangement of terms, into

$$\begin{aligned} E^{KS} &= \sum_{\mu\nu}(T_{\mu\nu} + V_{\mu\nu}^{KB})\rho_{\nu\mu} + \frac{1}{2}\sum_{IJ} U_{IJ}^{NA}(R_{IJ}) + \sum_{I<J}\delta U_{IJ}^{local}(R_{IJ}) - \sum_I U_I^{local} \\ &+ \int V^{NA}(\mathbf{r})\delta\rho(\mathbf{r})d^3\mathbf{r} + \frac{1}{2}\int \delta V^H(\mathbf{r})\delta\rho(\mathbf{r})d^3\mathbf{r} + \int \epsilon^{xc}(\mathbf{r})\rho(\mathbf{r})d^3\mathbf{r} \end{aligned}$$

where $V^{NA} = \sum_I V_I^{NA}$ and $\delta\rho = \rho - \sum_I \rho_I^{NA}$.

$$U_{IJ}^{NA}(R) = \int V_I^{NA}(\mathbf{r})\rho_J^{NA}(\mathbf{r}-\mathbf{R})d^3\mathbf{r} = -\frac{1}{4\pi}\int V_I^{NA}(\mathbf{r})\nabla^2 V_J^{NA}(\mathbf{r}-\mathbf{R})d^3\mathbf{r} \tag{47}$$

is a radial pairwise potential that can be obtained from $V_I^{NA}(r)$ as a two-center integral, by the same method described previously for the kinetic matrix elements:

$$T_{\mu\nu} = \langle \phi_\mu | -\frac{1}{2}\nabla^2 | \phi_\nu \rangle = -\frac{1}{2}\int \phi_\mu^*(\mathbf{r}) \nabla^2 \phi_\nu(\mathbf{r} - \mathbf{R}_{\mu\nu}) d^3\mathbf{r} \tag{48}$$

$V_{\mu\nu}^{KB}$ is also obtained by two-center integrals:

$$V_{\mu\nu}^{KB} = \sum_\alpha \langle \phi_\mu | \chi_\alpha \rangle v_\alpha^{KB} \langle \chi_\alpha | \phi_\nu \rangle \tag{49}$$

where the sum is over all the KB projectors χ_α that overlap simultaneously with ϕ_μ and ϕ_ν.

The last three terms in Eq. (47) are calculated using the real space grid. In addition to getting rid of all long-range potentials (except that implicit in $\delta V^H(\mathbf{r})$), the advantage of (47) is that, apart from the relatively slowly-varying exchange-correlation energy density, the grid integrals involve $\delta\rho(\mathbf{r})$, which is generally much smaller than $\rho(\mathbf{r})$. Thus, the errors associated with the finite grid spacing are drastically reduced. Critically, the kinetic energy matrix elements can be calculated almost exactly, without any grid integrations.

It is frequently desirable to introduce a finite electronic temperature T and/or a fixed chemical potential μ, either because of true physical conditions or to accelerate the self-consistency iteration. Then, the functional that must be minimized is the free energy [44]

$$\begin{aligned} F(\mathbf{R}_I, \psi_i(\mathbf{r}), n_i) = {} & E^{KS}(\mathbf{R}_I, \psi_i(\mathbf{r}), n_i) - \mu \sum_i n_i \\ & - k_B T \sum_i (n_i \log n_i + (1 - n_i)\log(1 - n_i)). \end{aligned} \tag{50}$$

The functional is built in such a way that minimization with respect to n_i yields the usual Fermi-Dirac distribution $n_i = 1/(1 + e^{(\epsilon_i - \mu)/k_B T})$.

9. Atomic forces and stress

Atomic forces and stresses are obtained by direct differentiation of (47) with respect to atomic positions (at finite temperture, really corresponding to the derivatives of the free energy). They are obtained simultaneously with the total energy, mostly in the same places of the code, under the general paradigm "a piece of energy ⇒ a piece of force/stress" (except that some pieces are calculated only in the last self-consistency step). This ensures that all contributions, including Pulay corrections, are automatically included.

The force contribution from the first term in (47) is

$$\begin{aligned} \frac{\partial}{\partial \mathbf{R}_I} \quad & \sum_{\mu\nu} (T_{\mu\nu} + V_{\mu\nu}^{KB}) \rho_{\nu\mu} = \sum_{\mu\nu} (T_{\mu\nu} + V_{\mu\nu}^{KB}) \frac{\partial \rho_{\nu\mu}}{\partial \mathbf{R}_I} + 2 \sum_\mu \sum_{\nu \in I} \frac{dT_{\mu\nu}}{d\mathbf{R}_{\mu\nu}} \rho_{\nu\mu} \\ & + 2 \sum_\mu \sum_{\nu \in I} \sum_\alpha S_{\mu\alpha} v_\alpha^{KB} \frac{dS_{\alpha\nu}}{d\mathbf{R}_{\alpha\nu}} \rho_{\nu\mu} - 2 \sum_{\mu\nu} \sum_{\alpha \in I} S_{\mu\alpha} v_\alpha^{KB} \frac{dS_{\alpha\nu}}{d\mathbf{R}_{\alpha\nu}} \rho_{\nu\mu} \end{aligned}$$

where α are KB projector indices, $\in I$ indicates orbitals or KB projectors belonging to atom I, and we have considered that

$$\frac{\partial S_{\mu\nu}}{\partial \mathbf{R}_{I_\nu}} = -\frac{\partial S_{\mu\nu}}{\partial \mathbf{R}_{I_\mu}} = \frac{dS_{\mu\nu}}{d\mathbf{R}_{\mu\nu}}, \tag{51}$$

where $\mathbf{R}_{I_\mu}$ is the position of atom I_μ, to which orbital ϕ_μ belongs and $\mathbf{R}_{\mu\nu} = \mathbf{R}_{I_\nu} - \mathbf{R}_{I_\mu}$.

Leaving aside for the moment the terms containing $\partial\rho_{\nu\mu}/\partial\mathbf{R}_I$, the other derivatives can be obtained by straightforward differentiation of their expansion in spherical harmonics (Eq. (24)). However, instead of using the spherical harmonics $Y_{lm}(\hat{\mathbf{r}})$ themselves, it is convenient to multiply them by r^l, in order to make them analytic at the origin. Thus

$$\begin{aligned} \frac{dS_{\mu\nu}(\mathbf{R})}{d\mathbf{R}} &= \sum_{lm} \nabla \left(\frac{S^{\mu\nu}_{lm}(R)}{R^l} R^l Y_{lm}(\hat{\mathbf{R}}) \right) \\ &= \sum_{lm} \frac{d}{dR} \left(\frac{S^{\mu\nu}_{lm}(R)}{R^l} \right) R^l Y_{lm}(\hat{\mathbf{R}}) \hat{\mathbf{R}} + \sum_{lm} \frac{S^{\mu\nu}_{lm}(R)}{R^l} \nabla (R^l Y_{lm}(\hat{\mathbf{R}})) \end{aligned} \qquad (52)$$

In fact, it is $S^{\mu\nu}_{lm}(R)/R^l$, rather than $S^{\mu\nu}_{lm}(R)$, that is stored as a function of R on a radial grid. Its derivative, $d(S^{\mu\nu}_{lm}(R)/R^l)/dR$, is then obtained from the same cubic spline interpolation used for the value itself. The value and gradient of $R^l Y_{lm}(\hat{\mathbf{R}})$ are calculated analytically from explicit formulae (up to $l = 2$) or recurrence relations [28]. Entirely analogous equations apply to $dT_{\mu\nu}/d\mathbf{R}_{\mu\nu}$.

The second and third terms in Eq. (47) are simple interatomic pair potentials whose force contributions are calculated trivially from their radial spline interpolations. The fourth term is a constant which does not depend on the atomic positions. Taking into account that $V^{NA}(\mathbf{r}) = \sum_I V^{NA}_I(\mathbf{r} - \mathbf{R}_I)$, and therefore $\partial V^{NA}(\mathbf{r})/\partial\mathbf{R}_I = -\nabla V^{NA}_I(\mathbf{r} - \mathbf{R}_I)$, the force contribution from the fifth term is

$$\frac{\partial}{\partial\mathbf{R}_I} \int V^{NA}(\mathbf{r})\delta\rho(\mathbf{r})d^3\mathbf{r} = -\int \nabla V^{NA}_I(\mathbf{r})\delta\rho(\mathbf{r})d^3\mathbf{r} + \int V^{NA}(\mathbf{r}) \frac{\partial\delta\rho(\mathbf{r})}{\partial\mathbf{R}_I} d^3\mathbf{r} \qquad (53)$$

The sixth term is the electrostatic self-energy of the charge distribution $\delta\rho(\mathbf{r})$:

$$\frac{\partial}{\partial\mathbf{R}_I} \frac{1}{2} \int \delta V^H(\mathbf{r})\delta\rho(\mathbf{r})d^3\mathbf{r} = \int \delta V^H(\mathbf{r}) \frac{\partial\delta\rho(\mathbf{r})}{\partial\mathbf{R}_I} d^3\mathbf{r} \qquad (54)$$

In the last term, we take into account that $d(\rho\epsilon^{xc})/d\rho = v^{xc}$ to obtain

$$\frac{\partial}{\partial\mathbf{R}_I} \int \epsilon^{xc}(\mathbf{r})\rho(\mathbf{r})d^3\mathbf{r} = \int V^{xc}(\mathbf{r}) \frac{\partial\rho(\mathbf{r})}{\partial\mathbf{R}_I} d^3\mathbf{r} \qquad (55)$$

Now, using Eq. (34) and that, for $\nu \in I$, $\partial\phi_\nu(\mathbf{r})/\partial\mathbf{R}_I = -\nabla\phi_\nu$, the change of the self-consistent and atomic densities are

$$\frac{\partial\rho(\mathbf{r})}{\partial\mathbf{R}_I} = \mathrm{Re} \sum_{\mu\nu} \frac{\partial\rho_{\nu\mu}}{\partial\mathbf{R}_I} \phi^*_\mu(\mathbf{r})\phi_\nu(\mathbf{r}) - 2\mathrm{Re} \sum_\mu \sum_{\nu\in I} \rho_{\nu\mu}\phi^*_\mu(\mathbf{r})\nabla\phi_\nu(\mathbf{r}) \qquad (56)$$

$$\frac{\partial\rho^{atom}(\mathbf{r})}{\partial\mathbf{R}_I} = -2\mathrm{Re} \sum_{\mu\in I} \rho^{atom}_{\mu\mu} \phi^*_\mu(\mathbf{r})\nabla\phi_\mu(\mathbf{r}) \qquad (57)$$

where we have taken into account that the density matrix of the separated atoms is diagonal. Thus, leaving still aside the terms with $\partial\rho_{\nu\mu}/\partial\mathbf{R}_I$, the last term in Eq. (53), as well as those in (54) and (55), have the general form

$$\mathrm{Re} \sum_\mu \sum_{\nu\in I} \rho_{\nu\mu} \int V(\mathbf{r})\phi^*_\mu(\mathbf{r})\nabla\phi_\nu(\mathbf{r})d^3\mathbf{r} = \mathrm{Re} \sum_\mu \sum_{\nu\in I} \rho_{\nu\mu} \langle\phi_\mu|V(\mathbf{r})|\nabla\phi_\nu\rangle. \qquad (58)$$

These integrals are calculated on the grid, in the same way as those for the total energy (i. e. $\langle \phi_\mu | V(\mathbf{r}) | \phi_\nu \rangle$). The gradients $\nabla \phi_\nu(\mathbf{r})$ at the grid points are obtained analytically, like those of $\phi_\nu(\mathbf{r})$ from their radial grid interpolations of $\phi(r)/r^l$:

$$\nabla \phi_{Ilmn}(\mathbf{r}) = \frac{d}{dr}\left(\frac{\phi_{Iln}(r)}{r^l}\right) r^l Y_{lm}(\hat{\mathbf{r}})\hat{\mathbf{r}} + \frac{\phi_{Iln}(r)}{r^l} \nabla (r^l Y_{lm}(\hat{\mathbf{r}})). \tag{59}$$

In some special cases, with elements that require hard partial core corrections or explicit inclusion of the semicore, the grid integrals may pose a problem for geometry relaxations, because they make the energy dependent on the position of the atoms relative to the grid. This 'eggbox effect' is small for the energy itself, and it decreases fast with the grid spacing. But the effect is larger and the convergence slower for the forces, as they are proportional to the amplitude of the energy oscillation, but inversely proportional to its period. These force oscillations complicate the force landscape, especially when the true atomic forces become small, making the convergence of the geometry optimization more difficult. Of course, the problem can be avoided by decreasing the grid spacing but this has an additional cost in computer time and memory. We have found it useful to minimize this problem by recalculating the forces using the grid-cell sampling described in section 6. This is equivalent to computing the forces averaging over a set of positions, determined by translating the whole system by a set of points in a finer mesh, and thus minimizing the error associated with the translational symmetry breaking.

We now turn to the force terms containing $\partial \rho_{\mu\nu}/\partial \mathbf{R}_I$. Substituting the first term of Eq. (56) into Eqs. (53-55) and adding the first term of Eq. (51) we obtain a simple expression that contains all those terms: $\sum_{\mu\nu} H_{\nu\mu} \partial \rho_{\mu\nu}/\partial \mathbf{R}_I$. The derivative of $\rho_{\mu\nu}$ with respect to the atomic positions is non-zero for atomic orbitals bases, since the orbitals move with the atoms, and the orthogonalization of the wave-functions must be imposed upon atomic displacements. It can be shown [6, 45] that this term can be expressed as:

$$\mathbf{F}_I^{orthog} = 2 \sum_\mu \sum_{\nu \in I} E_{\nu\mu} \frac{\partial S_{\mu\nu}}{\partial \mathbf{R}_{\mu\nu}} \tag{60}$$

where $E_{\mu\nu}$ is the so-called energy-density matrix:

$$E_{\mu\nu} = \frac{1}{2} \sum_{\eta\zeta} \left(S^{-1}_{\mu\eta} H_{\eta\zeta} \rho_{\zeta\nu} + \rho_{\mu\eta} H_{\eta\zeta} S^{-1}_{\zeta\nu} \right) = \sum_i c_{\mu i} n_i \epsilon_i c_{i\nu} \tag{61}$$

where ϵ_i are the eigenstate energies. This equation has been derived in different ways, and Ordejón et al [45] found it also for the $\mathcal{O}(N)$ functional, even though it does not require the occupied states to be orthogonal. In this case, Eq. (61) must be substituted by a more complicated expression [45].

The derivation of the stress formulas follows the same lines. We define the stress tensor as the positive derivative of the total energy with respect to the strain tensor

$$\sigma_{\alpha\beta} = \frac{\partial E^{KS}}{\partial \epsilon_{\alpha\beta}} \tag{62}$$

where α, β are Cartesian coordinate indices. To translate to standard units of pressure, we must simply divide by the unit-cell volume and change sign. During the deformation, all vector positions, including those of atoms and grid points (and of course lattice vectors), change according to

$$r'_\alpha = \sum_{\beta=1}^{3} \left(\delta_{\alpha\beta} + \epsilon_{\alpha\beta}\right) r_\beta \tag{63}$$

The shape of the basis functions, KB projectors, and atomic densities and potentials do not change, but their origin gets displaced according to (63). From this equation, we find that

$$\frac{\partial r_\gamma}{\partial \epsilon_{\alpha\beta}} = \delta_{\gamma\alpha} r_\beta \tag{64}$$

The change in E^{KS} is essentially due to these position displacements, and therefore the calculation of the stress is almost perfectly parallel to that of the atomic forces, thus being performed in the same sections of the code. For example:

$$\frac{\partial T_{\mu\nu}}{\partial \epsilon_{\alpha\beta}} = \sum_{\gamma=1}^{3} \frac{\partial T_{\mu\nu}}{\partial r^\gamma_{\mu\nu}} \frac{\partial r^\gamma_{\mu\nu}}{\partial \epsilon_{\alpha\beta}} = \frac{\partial T_{\mu\nu}}{\partial r^\alpha_{\mu\nu}} r^\beta_{\mu\nu} \tag{65}$$

Since $\partial T_{\mu\nu}/\partial r^\alpha_{\mu\nu}$ is evaluated to calculate the forces, it takes very little extra effort to multiply it also by $r^\beta_{\mu\nu}$ for the stress. Equally, force contributions like (58) have their obvious stress counterpart

$$\sum_{\mu\nu} \rho_{\nu\mu} \langle \phi_\mu | V(\mathbf{r}) | (\nabla_\alpha \phi_\nu) r_\beta \rangle \tag{66}$$

However, there are three exceptions to this parallelism. The first concerns the change of the volume per grid point or, in other words, the Jacobian of the transformation (63) in the integrals over the unit cell. This Jacobian is simply $\delta_{\alpha\beta}$, and it leads to a stress contribution

$$\left[\int \left(V^{NA}(\mathbf{r}) + \frac{1}{2}\delta V^H(\mathbf{r})\right) \delta\rho(\mathbf{r}) d^3\mathbf{r} + E^{xc}\right] \delta_{\alpha\beta} \tag{67}$$

Notice that the the renormalization of the density, required to conserve the charge when the volume changes, enters through the orthonormality constraints, and yields to a contribution to the stress:

$$\sigma^{orthog}_{\alpha\beta} = -\sum_{\mu\nu} E_{\nu\mu} \frac{\partial S_{\mu\nu}}{\partial R^\alpha_{\mu\nu}} R^\beta_{\mu\nu} \tag{68}$$

The second special contribution to the stress lies in the fact that, as we deform the lattice, there is a change in the factor $1/|\mathbf{r} - \mathbf{r}'|$ of the electrostatic energy integrals. We deal with this contribution in reciprocal space, when we calculate the Hartree potential by FFTs, by evaluating the derivative of the reciprocal-space vectors with respect to $\epsilon_{\alpha\beta}$. Since $G'_\alpha = \sum_\beta G_\beta(\delta_{\beta\alpha} - \epsilon_{\beta\alpha})$:

$$\frac{\partial}{\partial \epsilon_{\alpha\beta}} \frac{1}{G^2} = \frac{2 G_\alpha G_\beta}{G^4} \tag{69}$$

The third special stress contribution arises in GGA exchange and correlation, from the change of the gradient of the deformed density $\rho(\mathbf{r}) \to \rho(\mathbf{r}')$. The treatment of this contribution is explained in detail in reference [40].

10. Order-N functional

The basic problem for solving the Kohn-Sham equations in $\mathcal{O}(N)$ operations is that the solutions (the Hamiltonian eigenvectors) are extended over the whole system and overlap with each other.

Just to check the orthogonality of N trial solutions, by performing integrals over the whole system, involves $\sim N^3$ operations. Among the different methods proposed to solve this problem [4, 8], we have chosen the localized-orbital approach [46, 5, 47] because of its superior efficiency for non-orthogonal basis sets. The initially proposed functional [46, 5] used a fixed number of occupied states, equal to the number of electron pairs, and it was found to have numerous local minima in which the electron configuration was easily trapped. A revised functional form [47] which uses a larger number of states than electron pairs, with variable occupations, has been found empirically to avoid the local minima problem. This is the functional that we use and recommend.

Each of the localized, Wannier-like states, is constrained to its own localization region. Each atom I is assigned a number of states equal to $\text{int}(Z_I^{val}/2{+}1)$ so that, if doubly occupied, they can contain at least one excess electron (they can also become empty during the minimization of the energy functional). These states are confined to a sphere of radius R_c (common to all states) centered at $\mathbf{R}_I$. More precisely, the expansion (Eq. (31)) of a state ψ_i centered at $\mathbf{R}_I$ may contain only basis orbitals ϕ_μ centered on atoms J such that $|\mathbf{R}_{IJ}| < R_c$. This implies that $\psi_i(\mathbf{r})$ may extend to a maximum range $R_c + r_c^{max}$, where r_c^{max} is the maximun range of the basis orbitals. For covalent systems, a localization region centered on bonds rather than atoms is more efficient [48] (it leads to a lower energy for the same R_c), but it is less suitable to a general algorithm, especially in case of ambiguous bonds. Therefore, we generally use the atom-centered localization regions.

In the method of Kim, Mauri, and Galli (KMG) [47], the band-structure energy is rewritten as:

$$\begin{aligned} E^{KMG} &= 2\sum_{ij}(2\delta_{ji} - S_{ji})(H_{ij} - \eta S_{ij}) \\ &= 4\sum_i\sum_{\mu\nu} c_{i\mu}\delta H_{\mu\nu}c_{\nu i} - 2\sum_{ij}\sum_{\alpha\beta\mu\nu} c_{i\alpha}S_{\alpha\beta}c_{\beta j}c_{j\mu}\delta H_{\mu\nu}c_{\nu i} \end{aligned} \tag{70}$$

Where $S_{ij} = \langle\psi_i|\psi_j\rangle$, $H_{ij} = \langle\psi_i|H|\psi_j\rangle$, $\delta H_{\mu\nu} = H_{\mu\nu} - \eta S_{\mu\nu}$, and we have assumed a non-magnetic solution with doubly occupied states. The 'double count' correction terms of Eq. (41) remain unchanged and the electron density is still defined by (34), but the density matrix is re-defined as

$$\rho_{\mu\nu} = 2\sum_{ij} c_{\mu i}(2\delta_{ij} - S_{ij})c_{j\nu} = 4\sum_i c_{\mu i}c_{i\nu} - 2\sum_{ij}\sum_{\alpha\beta} c_{\mu i}c_{i\alpha}S_{\alpha\beta}c_{\beta j}c_{j\nu} \tag{71}$$

The parameter η in Eq. (70) plays the role of a chemical potential, and must be chosen to lie within the band gap between the occupied and empty states. This may be tricky sometimes, since the electron bands can shift during the self-consistency process or when the atoms move. In general, the number of electrons will not be exactly the desired one, even if η is within the band gap, because the minimization of (70) implies a trade-off in which the localized states become fractionally occupied. To avoid an infinite Hartree energy in periodic systems, we simply renormalize the density matrix so that the total electron charge $\sum_{\mu\nu} S_{\mu\nu}\rho_{\nu\mu}$ equals the required value.

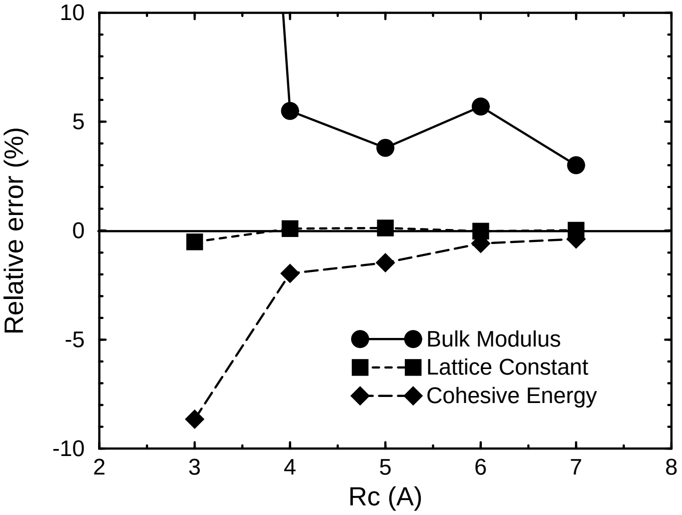

Figure 6: Convergence of the lattice constant, bulk modulus, and cohesive energy as a function of the localization radius R_c of the Wannier-like electron states in silicon. We used a supercell of 512 atoms and a minimal basis set with a cutoff radius $r_c = 5$ a.u. for both s and p orbitals.

For a given potential, the functional (70) is minimized by the conjugate-gradients method, using its derivatives with respect to the expansion coefficients

$$\frac{\partial E^{KMG}}{\partial c_{i\mu}} = 4\sum_{\nu} \delta H_{\mu\nu} c_{\nu i} - 2\sum_{j}\sum_{\alpha\beta\nu} (S_{\mu\nu} c_{\nu j} c_{j\alpha} \delta H_{\alpha\beta} c_{\beta i} + \delta H_{\mu\nu} c_{\nu j} c_{j\alpha} S_{\alpha\beta} c_{\beta i}) \qquad (72)$$

The minimization proceeds without need to orthonormalize the electron states ψ_i. Instead, the orthogonality, as well as the correct normalization (one below η and zero above it) result as a consequence of the minimization of E^{KMG}. This is because, in contrast to the KS functional, E^{KMG} is designed to penalize any nonorthogonality [47]. The KS ground state, with all the occupied ψ_i's orthonormal, is also the minimum of (70), at which $E^{KMG} = E^{KS}$. If the variational freedom is constrained by the localization of the ψ_i's, the orthogonality cannot be exact, and the resulting energy is slightly larger than for unconstrained wavefunctions. In insulators and semiconductors, the Wannier functions are exponentially localized [49], and the energy excess due to their strict localization decreases rapidly as a function of the localization radius R_c, as can be seen in Fig. 6.

If the system is metallic, or if the chemical potential is not within the band gap (for example because of the presence of defects), the KMG functional cannot be used in practice. In fact, although some $\mathcal{O}(N)$ methods can handle metallic systems in principle [8], we are not aware of any practical calculations at a DFT level. In such cases we copy the Hamiltonian and overlap matrices to standard expanded arrays and solve the generalized eigenvalue problem by conventional order-N^3 diagonalization techniques [50]. However, even in this case, most of the operations, and particularly those to find the density and potential, and to set up the Hamiltonian, are still performed in $\mathcal{O}(N)$ operations.

Table 3: Average number of selfconsistency (SCF) iterations (per molecular dynamics step) and average number of conjugate-gradient (CG) iterations (per SCF iteration) required to minimize the $\mathcal{O}(N)$ functional, during a simulation of bulk silicon at ~ 300 K. We used the Verlet method [53] at constant energy, with a time step of 1.5 fs, and a minimal basis set with a cutoff radius $r_c = 5$ a.u. R_c is the localization radius of the Wannier-like wavefunctions used in the $\mathcal{O}(N)$ functional (see text). N is the number of atoms in the system.

	$R_c = 4$Å		$R_c = 5$Å	
N	CG	SCF	CG	SCF
64	5.8	9.3	8.4	8.4
512	4.9	11.4	8.8	10.1
1000	4.3	11.5	9.9	11.5

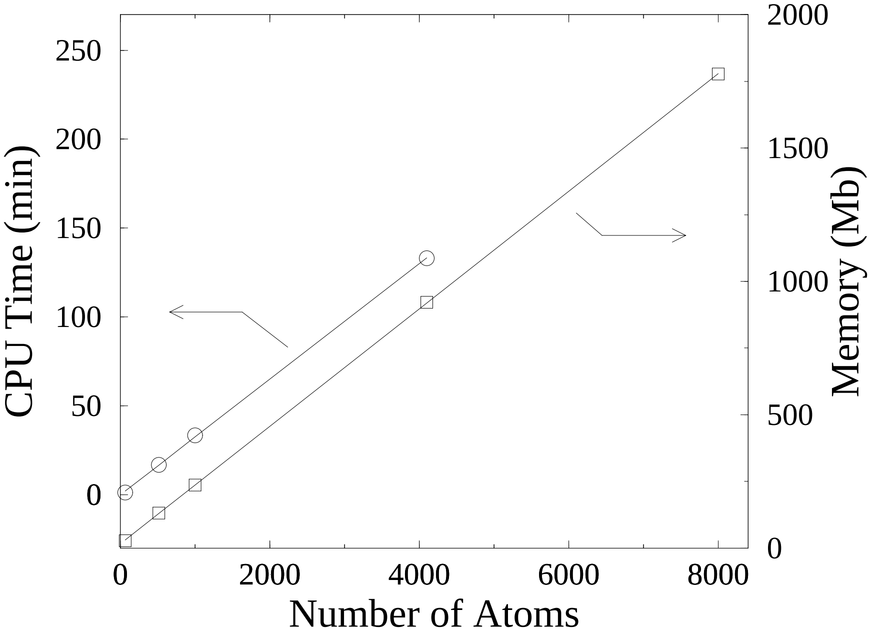

Figure 7: CPU time and memory for silicon supercells of 64, 512, 1000, 4096, and 8000 atoms. Times are for one average molecular dynamics step at 300 K. This includes 10 SCF steps, each with 10 conjugate gradient minimization steps of the $\mathcal{O}(N)$ energy functional. Memories are peak ones. Although the memory requierement for 8000 atoms was determined accurately, the run could not be performed because of insufficient memory in the PC used.

Irrespective of whether the $\mathcal{O}(N)$ functional or the standard diagonalization is used, an outer selfconsistency iteration is required, in which the density matrix is updated using Pulay's Residual Metric Minimization by Direct Inversion of the Iterative Subspace (RMM-DIIS) method [51, 52]. Even when the code is strictly $\mathcal{O}(N)$, the CPU time may increase faster if the number of iterations required to achieve the solution increases with N. In fact, it is a common experience that the required number of selfconsistency iterations increases with the size of the system. This is mainly because of the 'charge sloshing' effect, in which small displacements of charge from one side of the system to another give rise to larger changes of the potential, as the size increases. Fortunately, the localized character of the Wannier-like wavefunctions used in the $\mathcal{O}(N)$ method help to solve also this problem, by limiting the charge sloshing. Table 3 presents the average number of iterations required to minimize the $\mathcal{O}(N)$ functional and the average number of selfconsistency iterations, during a molecular dynamics simulation of bulk silicon at room temperature. It can be seen that these numbers are quite small and that they increase very moderately with system size. As might be expected, the number of minimization iterations increase with the localization radius, i.e. with the number of degrees of freedom ($c_{\mu i}$ coefficients) of the wavefunctions. But this increase is also rather moderate.

Figure 7 shows the essentially perfect $\mathcal{O}(N)$ behaviour of the overall CPU time and memory. This is not surprising in view of the completely strict enforcement of $\mathcal{O}(N)$ algorithms everywhere in the code (except the marginal $N \log N$ factor in the FFT used to solve Poisson's equation, which represents a very small fraction of CPU time even for 4000 atoms).

11. Other features

Here we will simply mention some of the possibilities and features of the SIESTA implementation of DFT:

- The most recent version of SIESTA is partially writen in Fortran-90, and implements dynamical memory allocation, so that the same executable can be used for any system under study. Also, parallelization has been achieved using MPI. In benchmark calculations performed on an SGI Origin computer, using the Kim *et al.* Order-N functional, a system with 131,072 silicon atoms was solved using 64 processors.

- A general-purpose package [54], the flexible data format (fdf), initially developped for the SIESTA project, allows the introduction of all the data and precision parameters in a simple tag-oriented, order-independent format which accepts different physical units. The data can then be accessed from anywhere in the program, using simple subroutine calls in which a default value is specified for the case in which the data are not present. A simple call also allows the read pointer to be positioned in order to read complex data 'blocks' also marked with tags.

- Non-collinear spin polarized systems [55, 56, 57] can be studied with SIESTA [58]. The spin direction is defined in the real space grid points, and therefore no atomic sphere approximation is used.

- The systematic calculation of atomic forces and stress tensor allows the simultaneous relaxation of atomic coordinates and cell shape and size, using a conjugate gradients minimization or several other minimization/annealing algorithms.

- It is possible to perform a variety of molecular dynamics simulations, at constant energy or temperature, and at constant volume or pressure, also including Parrinello-Rahman dynamics with variable cell shape [53]. The geometry relaxation may be restricted, to impose certain positions or coordinates, or more complex constraints.
- The auxiliary program VIBRA processes systematically the atomic forces for sets of displaced atomic positions, and from them computes the Hessian matrix and the phonon spectrum. An interface to the PHONON program [59] is also provided within SIESTA.
- A linear response program (LINRES) to calculate phonon frequencies has also been developed [60]. The code reads the SCF solution obtained by Siesta, and calculates the linear response to the atomic displacements, using first order perturbation theory. It then calculates the dynamical matrix, from which the phonon frequencies are obtained.
- The calculation of the electric polarization, as an integral in the grid across the unit cell, is standard and almost free for molecules, chains and slabs (in the directions perpendicular to the chain axis, or to the surface). For bulk systems, the electric polarization cannot be found from the charge distribution in the unit cell alone. In this case, we use the so-called Berry-phase theory of polarization [61, 62], which we have implemented in SIESTA [63]. This allows us to compute quantities like the dynamical charges [61] and piezoeletric constants [64, 65].
- A number of auxiliary programs allows various representations of the total density, the total and local density of states, and the electrostatic or total potentials. The representations include both two-dimensional cuts and three-dimensional views, which may be colored to simultaneously represent the density and potential.
- Thanks to an interface with the TRANSIESTA program, it is posible to calculate transport properties across a nanocontact, finding self-consistently the effective potential across a finite voltage drop, at a DFT level, using the Keldish Green's function formalism [66].
- The optical response can be studied with SIESTA using different approaches. An approximate dielectric function can be calculated from the dipolar transition matrix elements between occupied and unoccupied single-electron eigenstates using first order time-dependent pertubation theory [67]. For finite systems, these are easily calculated from the matrix elements of the position operator between the basis orbitals. For infinite periodic systems, we use the matrix elements of the momentum operator. It is important to notice, however, that the use of non-local pseudopotentials requires some correction terms [68]. We have also implemented a more sophisticated approach to compute the optical response of finite systems, using the adiabatic approximation to time-dependent DFT [69, 70]. The idea is to integrate the time-dependent Schrödinger equation when a time depedent perturbation is applied to the system [71]. From the time evolution, it is then possible to extract the optical adsorption and dipole strength functions, including some genuinely many-body

effects, like plasmons. Using this approach we have succesfully calculated the electronic response of systems such as fullerenes and small metallic clusters [72].

12. Some applications to benchmark systems

12.1 Ferroelectric perovskites

DFT calculations are making a big impact is the study of ferroelectric materials, and in particular, ferroelectric perovskite oxides. The combination of accurate DFT calculations with Monte Carlo approaches are allowing to advance very significantly in understanding the basic physics of the ferroelectric transition in these systems. However, the advance in this field has been limited by the fact that the relevant energies involved in the ferroelectric distortions are very small, and therefore very accurate calculations are required to produce reasonable results [73, 74]. This poses a problem even for standard methods like pseudopotential-plane-waves, because of the important role played by the semicore states, which must be included explicitly in the calculation and makes it very costly, since very large plane-waves cutoff are needed to describe these states.

Due to these difficulties and the high computational cost, only the simplest ferroelectric perovskites have been studied so far by means of first principles methods. More complex and technologically more important materials, or complex combinations of these (heterostructures, thin films, etc) are therefore quite out of reach so far. It seems obvious that a method which would produce the accuracy necessary while keeping a low computational cost would be of great importance in this field. Here we present results for $BaTiO_3$ that show that SIESTA is able to provide such accuracy for a variety of properties such as lattice constant, energy surfaces, phonon frequencies and effective Born charges.

The calculations presented here were done as follows. We have used the LDA functional of Perdew and Zunger. Due to the importance of semi-core states, the $3s$ and $3p$ electrons of Ti and the $5s$ and $5p$ of Ba were included explicitly in the calculation. The Troullier-Martins [22] pseudopotentials were generated with those states in the valence, and with the following reference configurations: $3s^2 3p^6 3d^2$ for Ti^{+2}, $5s^2 5p^6$ for Ba^{+2} and $2s^2 2p^4$ for O. The radii used were: for Ti, 1.3 a.u for the s, p and d states, and 2.0 for the f states; for Ba, 1.75, 2.0, 2.5 and 2.5 a.u. for the s, p, d and f states, respectively; and for O, 1.15 a.u. for the s, p and d states and 1.5 a.u. for the f states. The basis set used here was single-ζ for the semicore states of Ti and Ba, and double-ζ plus a single shell of polarization functions for the valence states of all atoms. For Ba, an extra single shell of $5d$ orbitals was added. This amounts to a total of 19 orbitals for Ti, 14 orbitals for Ba and 13 orbitals for O.

To obtain the integrals of the Hamiltonian that are computed on a real space grid, we have used an equivalent cutoff of 200 Ry to represent the charge density. Once self-consistency was achieved, the grid was refined (reducing the spacing between grid points by half) to compute the total energy, atomic forces and stress. The sampling of reciprocal space was done using a $(6 \times 6 \times 6)$ Monkhorst-Pack mesh. Although $BaTiO_3$ is an insulator, it has been shown that this large sampling is necessary to reproduce properly the energetics of the system [73, 74].

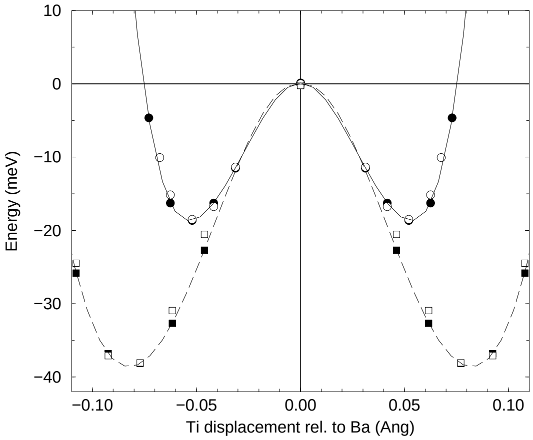

Figure 8: Energy versus distortion for cubic $BaTiO_3$, for tetragonal (circles) and rhombohedral (squares) distortions. The full symbols are the results of SIESTA, whereas the open symbols are the FPLAPW results. The patterns of the distortions were taken from the experiment. The calculations were done at the experimental lattice constant. The lines are fit to the results of SIESTA, to guide the eye. Energies are referred to that of the cubic phase at the experimental lattice constant.

We have first considered the undistorted cubic phase. We obtain an equilibrium lattice constant of 7.46 a.u., very close to previous LDA results from LAPW (7.45 a.u.) [75] or with plane-waves (7.456 a.u.) [73] calculations. The LDA results underestimate significantly the lattice constant of the cubic phase, which experimentally is found to be 7.57 a.u.

We have next considered the energy gain for a ferroelectric distortion. At high temperature, $BaTiO_3$ shows a cubic symmetry with no net polarization. Upon lowering the temperature, three ferroelectric transitions appear: first, to a tetragonal, then an orthorombic and finally a rhombohedral phase. We have calculated the energy as a function of ferroelectric displacement for two different distortions: the rhombohedral and the tetragonal. In the calculation, we have used a cubic cell with a lattice constant at the experimental value, although experimentally the unit cell is found to deform slightly according to the symmetry of the ferroelectric distortion. We will neglect this deformation, since our goal is to validate the results of SIESTA by comparing them with benchmark DFT calculations. To that end, we use the FPLAPW method [76, 77], which is the most accurate DFT approach which can be used to study these systems. The comparison is presented in Figure 8, which shows the energy as a function of the displacement of the Ti atom (the distortion vector is taken from the experiment [78]). We can observe that the agreement between both methods is excellent. Both calculations are able to reproduce the minimum of the energy for a value of the distortion parameter very close to the experimental one. The energy gain in the rhombohedral phase is more than twice as much as that of the tetragonal phase. This is consistent with the experiment, where the tetragonal phase occurs at higher temperature than the rhombohedral one, which is the low temperature stable phase.

Many of the features of the ferroelectric behavior of $BaTiO_3$ can be explained by looking at the phonon structure of the undistorted cubic phase. The appearance of unstable modes (with

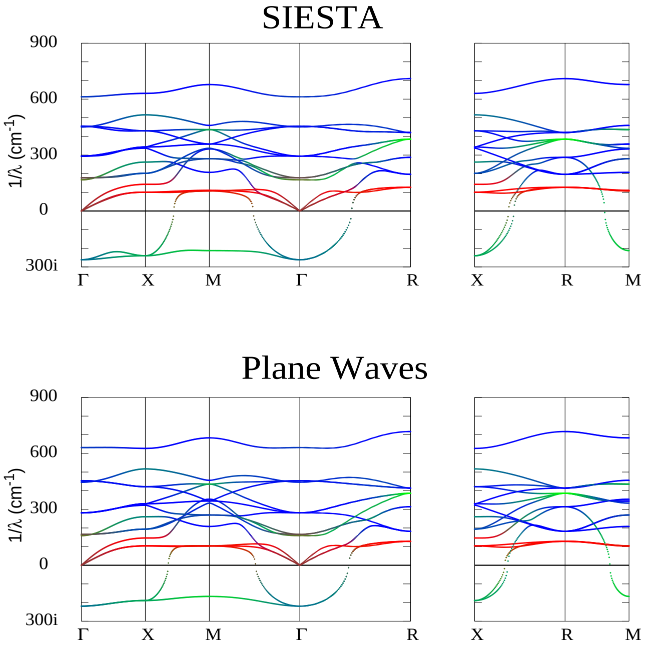

Figure 9: Phonon dispersion relations for cubil $BaTiO_3$, calculated with Siesta (top panel) and with plane waves (taken from [79]). The colors indicate the main atoms that participate in each vibration: blue, green and red correspond to O, Ti and Ba, respectively. Unstable modes are indicated by imaginary frequencies.

imaginary frequency) indicate the presence of instabilities which cause the ferroelectric transitions. Figure 9 shows a plot of the phonon spectra of cubic $BaTiO_3$, computed with Siesta (upper panel) and with plane-waves (lower panel) [79]. We see that the agreement is very good. In particular, Siesta is able to reproduce all the unstable branches throughout the Brillouin zone. The colors represent the character of each mode: blue, green and red correspond to O, Ti and Ba displacements, respectively. Both the frequencies and the character of all modes are well described with Siesta.

We have also computed the Born effective charges of the cubic phase. These are important because they determine the value of the polarization for a ferroelectric distortion, as well as other properties such as the IR response, or the LO-TO splitting. The symmetry of the cubic $BaTiO_3$ phase reduces the number of nonzero elements of the dynamical charge tensor to four: Z*(Ti) and Z*(Ba) for the two metal atoms (their effective charge tensor is isotropic), and $Z^*(O_I)$ and $Z^*(O_{II})$ for the oxygen, corresponding to displacements parallel or normal to BaO planes. We have calculated the Born charges by finite differences, using the Berry phase method [61, 62] implemented in Siesta [63], to compute the net polarization of the system for finite values of the atomic displacements. These were taken as about 0.3% of the value of the lattice constant. We used a $(4 \times 4 \times 20)$ k-point grid, to allow for a larger number of k-points in the direction of the atomic displacement. We summarize our results in table 4, together with those obtained with plane-waves calculations by other authors [80, 81]. Again, we find good agreement, although the differences between our results and those of plane waves are larger (but comparable) to those between different plane-waves calculations. As with plane-waves, we find

Table 4: Born charges for cubic $BaTiO_3$ computed with SIESTA and with plane waves [80, 81].

	SIESTA	PW [80]	PW [81]
Ba	2.72	2.77	2.75
Ti	7.60	7.25	7.16
O_{II}	-2.18	-2.15	-2.11
O_I	-5.96	-5.71	-5.69

values quite larger than the nominal valences of the atoms in the compound, pointing out the importance of covalency in this material.

12.2 Molecular systems

Here, we show some results of a thorough study of the ability of SIESTA to tackle complex organic and inorganic molecules [82]. In these calculations, we used a double-ζ basis set plus a single shell of polarization orbitals on all the atoms. The radii of the orbitals were obtained using an energy shift parameter of 0.005 Ry, resulting in relatively long orbitals. Troullier-Martins pseudopotentials [22], and the GGA functional of Perdew, Burke and Erzenhof [12] were used. The real space integrals grid cutoff was set to 150 Ry.

In a first study, we focus on the structure of a set of 103 molecules. For details, the complete list of molecules is available (http://uqbar.ncifcrf.gov/˜rcachau/Siesta). The set was selected to include some of the most difficult cases reported in the evaluation of semiempirical methods as well as highly stressed (e.g. very polar bonds) and very similar (e.g. alcohol series) geometries for sensitivity analysis. They also include several H-bonded complexes. We compare our results with those obtained from calculations using gaussian basis sets, with the B3LYP functional [83], and with semiempirical methods like AM1 and PM3 [84]. B3LYP, AM1 and PM3 calculations were performed using Gaussian 98 A.7 [85] with 6311G(2d,2p) atomic basis sets and standard cutoffs for SCF, and geometry optimization. All semiempirical (AM1 and PM3) calculations were performed using the amide molecular mechanics correction where required.

Figure 10 shows a comparison of the geometries obtained with the different methods. The bond angles and bond distances were selected to exclude symmetry related redundancy. Note the extremely good correlation between SIESTA and B3LYP calculations. The correlation of B3LYP geometries with experimental values is well known, and also translates to the SIESTA geometries. The bond distances were presented as squared values to expand the scale. This helps observe the clustered aspect of the semiempirical plots (not observed in the SIESTA vs. B3LYP correlations), which is a direct result of the parametrization procedure. More details of these results can be found in Ref. [82] and http://uqbar.ncifcrf.gov/˜rcachau/Siesta).

In a second test case [86], we will discuss the description of H-bonds and the comparison with the results of accurate quantum-chemical second-order Moller-Plesset (MP2) calculations . In particular, we will focus on the study of DNA base pairs due to their biological relevance and the availability of extensive MP2 calculations [87]. H-bonding interactions are of paramount

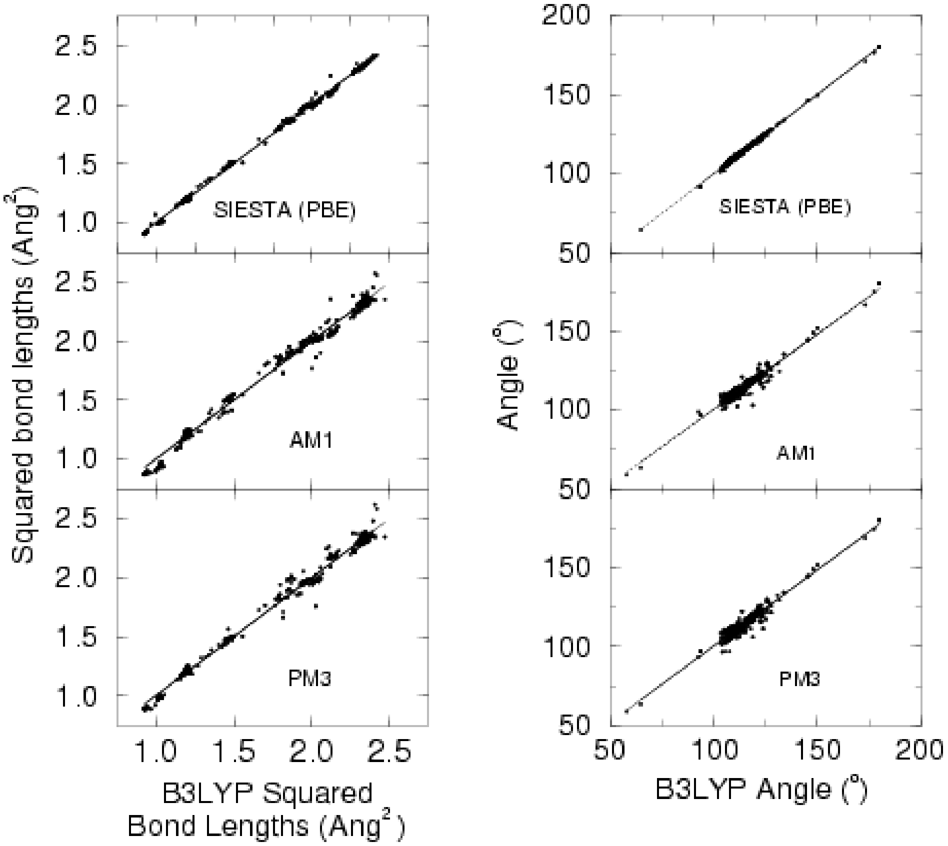

Figure 10: Comparison of the squared bond distances (left) and bond angles (right) between the B3LYP results and those of SIESTA and the semiempirical AM1 and PM3 methods, for the database of 103 organic and inorganic molecules.

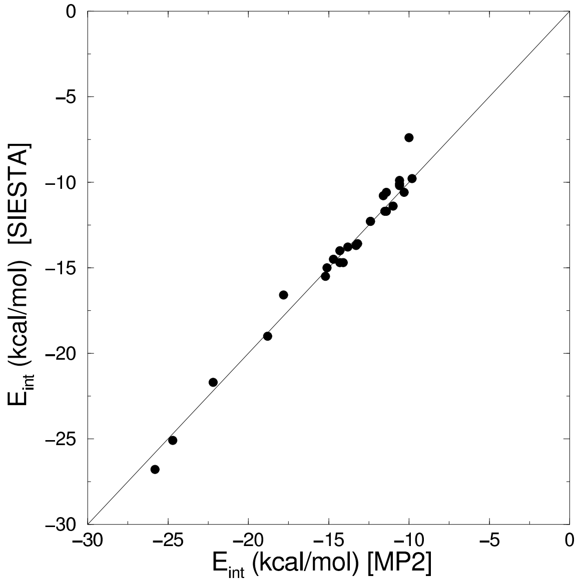

Figure 11: Binding energies of a set of 30 DNA base-pairs, comparing the results obtained with SIESTA with those of MP2 calculations (by Sponer et al. [87])

importance in the description of DNA systems, among the many factors that stabilize the double helix. In order to validate the capability of SIESTA to describe DNA, we considered first the interactions between nitrogenated base pairs (adenine, guanine, thymine and cytosine). A thorough study of 30 nucleic acid pairs was performed, addressing the precision of the approximations (basis sets, grids, etc) and the accuracy of the GGA functional. Our calculations, presented in detail elsewhere [86], show that the PBE functional [12] provides excellent results. In figure 11 we show a comparison of the binding energies (difference between the energy of the H-bonded pair and the free bases) for 30 different base pairs, with those obtained by Sponer et al. [87], by means MP2 calculations. In both cases, the coordinates were the same: those obtained by Sponer and co-workers at the Hartree-Fock level (due to the numerical workload, it was not possible to optimize the structures at the MP2 level). The results of figure 11 show that the correlation of the energies obtained with SIESTA and those of MP2 are excellent, with an average deviation of only 0.73 kcal/mol. This is considerably better than the accuracy that can be expected from total energies in DFT, showing the very nice performance of the PBE functional for these systems, and validating SIESTA as an accurate method for the study of hydrogen bonds in DNA complexes. We have also performed structural optimizations with SIESTA to obtain the first geometries for many of the base-pairs under study. Former DFT works had only considered the structures of the most common Watson-Crick base-pairs. For these, our result agree closely (always within 2% for the bonding distances at the H-bonds) with those of previous calculations. Further details can be found on [86].

13. Conclusions

The SIESTA approach for DFT calculations has been thoroughly described, with illustrations of the convergence with respect to the main precision parameters that characterize the method. We have shown that the method is able to produce very fast calculations with small basis sets, allowing to compute systems a thousand of atoms in single processor workstations (and many more in parallel platforms). At the same time, the use of more complete and accurate bases allows to achieve accuracies comparable to those of standard plane waves calculations, still at an advantageous computational cost. We have shown some examples of the accuracy of the method, in the context of ferroelectric materials and molecular systems, although many others have been studied so far (see http://www.uam.es/siesta/). The capabilities, performance and flexibility of the method make it a very useful tool for the study of large molecules and complex, and we hope it will serve an increasing number of groups in our community.

ACKNOWLEDGMENTS

We are deeply indebted to Otto Sankey and David Drabold for allowing us to use their code as an initial seed for this project, and to Richard Martin for continuous ideas and support. We thank Jose Luis Martins for numerous discussions and ideas, and Jürgen Kübler for helping us implement the noncollinear spin. The exchange-correlation methods and routines were developed in collaboration with Carlos Balbas and Jose L. Martins. We also thank In-Ho Lee, Maider

Machado, Juana Moreno, and Art R. Williams for some routines, and Eduardo Anglada and Oscar Paz for their computational help. Part of the results presented here were obtained in collaboration with R. Weht, R. Cachau, M. Machado and Ph. Ghosez. This work was supported by the Fundación Ramón Areces and by Spain's MCyT grant BFM2000-1312. JDG would like to thank the Royal Society for a University Research Fellowship and EPSRC for the provision of computer facilities. PO thanks CESCA and CEPBA, coordinated by C^4, for providing their computing facilities. DSP acknowledges support from the Basque Government (Programa de Formación de Investigadores). This work has benefited from the collaboration within and was partially funded by the ESF Programme on "Electronic Structure Calculations for Elucidating the Complex Atomistic Behaviour of Solids and Surfaces". We gratefully acknowledge this continuous support.

References

[1] L. Greengard, Science, **265**, 909 (1994)

[2] R. W. Hockney and J. W. Eastwood, *Computer Simulation Using Particles*, IOP Publishing, Bristol, 1988.

[3] C. M. Goringe, D. R. Bowler and E. Hernandez, **60**, 1447 (1997)

[4] P. Ordejón, Comp. Mat. Sci. **12**, 157 (1998)

[5] P. Ordejón, D. A. Drabold, M. P. Grumbach and R. M. Martin, Phys. Rev. B **48**, 14646 (1993)

[6] O. F. Sankey and D. J. Niklewski, Phys. Rev. B, **40**, 3979 (1989)

[7] M. C. Payne, M. P. Teter, D. C. Allan, T. A. Arias and J. D. Joannopoulos, Rev. Mod. Phys. **64**, 1045 (1992)

[8] S. Goedecker, Rev. Mod. Phys. **71**, 1085 (1999)

[9] E. Hernandez and M. J. Gillan, Phys. Rev. B **51**, 10157 (1995)

[10] W. Kohn and L. J. Sham, Phys. Rev. **140**, 1133 (1965)

[11] J. P. Perdew and A. Zunger, Phys. Rev. B **23**, 5048 (1981)

[12] J. P. Perdew, K. Burke and M. Ernzerhof, Phys. Rev. Lett **77**, 3865 (1996)

[13] D. R. Hamann, M. Schlüter and C. Chiang, Phys. Rev. Lett. **43**, 1494 (1979)

[14] G. B. Bachelet, D. R. Hamann and M. Schlüter, Phys. Rev. B **26**, 4199 (1982)

[15] L. Kleinman and D. M. Bylander, Phys. Rev. Lett. **48**, 1425 (1982)

[16] S. G. Louie, S. Froyen and M. L. Cohen, Phys. Rev. B **26**, 1738 (1982)

[17] P. Ordejón, E. Artacho and J. M. Soler, Phys. Rev. B **53**, R10441 (1996)

[18] D. Sánchez-Portal, P. Ordejón, E. Artacho and J. M. Soler, Int. J. Quantum Chem. **65**, 453 (1997)

[19] P. Ordejón, phys. stat. sol (b) **217**, 335 (2000); See also http://www.uam.es/siesta

[20] L. Kleinman, Phys. Rev. B **21**, 2630 (1980)

[21] G. B. Bachelet and M. Schlüter, Phys. Rev. B **25**, 2103 (1982)

[22] N. Troullier and J. L. Martins, Phys. Rev. B **43**, 1993 (1991)

[23] P. E. Blöchl, Phys. Rev. B **41**, 5414 (1990)

[24] N. J. Ramer and A. M. Rappe, Phys. Rev. B **59**, 12471 (1999)

[25] David Vanderbilt, Phys. Rev. B **32**, 8412 (1985)

[26] The local potentials constructed in this way usually have a strength (depth) that is an average of the different V_l's and neither too deep nor too shallow. This tends to maintain the separable potentials free of ghost states (see X. Gonze, R. Stumpf and M. Scheffler, Phys. Rev. B **44**, 8503 (1991))

[27] If there are both semicore and valence electrons with the same angular momentum, the pseudopotential is generated for an ion.

[28] W. H. Press, S. A. Teukolsky, W. T. Vetterling and B. P. Flannery, *Numerical Recipes*, 2nd Edition, Cambridge University Press (Cambridge, 1992)

[29] D. Sánchez-Portal, J. M. Soler and E. Artacho, J. Phys.: Condens. Matter **8**, 3859 (1996)

[30] G. Lippert, J. Hutter, P. Ballone and M. Parrinello, J. Phys. Chem. **100**, 6231 (1996)

[31] E. Artacho, D. Sánchez-Portal, P. Ordejón, A. García and J. M. Soler, phys. stat. sol. (b) **215**, 809 (1999)

[32] S. Huzinaga and others, *Gaussian basis sets for molecular calculations*, Elsevier Science (Berlin, 1984)

[33] J. Junquera, O. Paz, D. Sánchez-Portal and E. Artacho, cond-mat/0104170. To appear in Phys. Rev. B

[34] C. Filippi, D. J. Singh and C. J. Umrigar, Phys. Rev. B **50**, 14947 (1994)

[35] C. Kittel, *Introduction to Solid State Physics*, John Wiley and Sons (New York, 1986)

[36] Some integrals, like $\langle\phi_{Ilmn}|V_I^{NA}|\phi_{I'l'm'n'}\rangle$ could also be calculated in this way, but this is not the case of $\langle\phi_{Ilmn}|V_{I''}^{NA}|\phi_{I'l'm'n'}\rangle$, which involve rather cumbersome three-center integrals of arbitary numerical functions [6]. Therefore, it is simpler to find the total neutral-atom potential and to calculate a single integral $\langle\phi_{Ilmn}|V^{NA}(\mathbf{r})|\phi_{I'l'm'n'}\rangle$ in the uniform spatial grid.

[37] J. D. Jackson, *Classical Electrodynamics*, John Wiley & Sons (New York, 1962)

[38] J. M. Soler, E. Artacho, J. Gale, A. García, J. Junquera, P. Ordejón and D. Sánchez-Portal, cond-mat/0111138

[39] Notice that our grid cutoff to represent the density is not directly comparable to the energy cutoff in the context of plane wave codes, which usually refers to the wavefunctions. Strictly speaking, the density requires a value four times larger.

[40] L. C. Balbas, J. L. Martins and J. M. Soler, Phys. Rev. B **64**, 165110 (2001)

[41] G. Makov and M. C. Payne, Phys. Rev. B **51**, 4014 (1995)

[42] J. Moreno and J. M. Soler, Phys. Rev. B, **45**, 13891 (1992)

[43] H. J. Monkhorst and J. D. Pack, Phys. Rev. B **13**, 5188 (1976)

[44] N. D. Mermin, Phys. Rev. **137**, 1441 (1965)

[45] P. Ordejón, D. A. Drabold, R. M. Martin and M. P. Grumbach, Phys. Rev. B **51**, 1456 (1995)

[46] F. Mauri, G. Galli and R. Car, Phys. Rev. B **47**, 9973 (1993)

[47] J. Kim, F. Mauri and G. Galli, Phys. Rev. B **52**, 1640 (1995)

[48] U. Stephan, D. A. Drabold and R. M. Martin Phys. Rev. B **58**, 13472 (1998)

[49] W. Kohn, Phys. Rev. **115**, 809 (1959)

[50] E. Anderson, Z. Bai, C. Bischof, L. S. Blackford, J. Demmel, J. Dongarra, J. Du Croz, A. Greenbaum, S. Hammarling, A. McKenney and D. Sorensen, *LAPACK Users' Guide*, 3rd Edition, SIAM (Philadelphia, 1999)

[51] P. Pulay, Chem. Phys. Lett. **73**, 393 (1980)

[52] P. Pulay, J. Comp. Chem. **13**, 556 (1982)

[53] M. P. Allen and D. J. Tildesley, *Computer Simulation of Liquids*, Oxford Univ. Press (Oxford, 1987)

[54] A. Garcia and J. M. Soler, *A Flexible Data Format for Physical Simulations*, unpublished.

[55] L. M. Sandratskii and P. G. Guletskii, J. Phys. F: Metal Phys. **16**, L43 (1986)

[56] J. Kübler, K. H. Höck, J. Sticht and A. R. Williams, J. Appl. Phys. **63**, 3482 (1988)

[57] T. Oda, A. Pasquarello and R. Car, Phys. Rev. Lett. **80**, 3622 (1998)

[58] A. V. Postnikov, P. Engel and J. M. Soler, cond-mat/0109540. Submitted to Phys. Rev. B

[59] K. Parlinski, unpublished.

[60] J. M. Pruneda, S. Estreicher, J. Junquera, J. Ferrer and P. Ordejón, cond-mat/0109306. To appear in Phys. Rev. B

[61] R. D. King-Smith and D. Vanderbilt, Phys. Rev. B **47**, 1651 (1993)

[62] R. Resta, Rev. Mod. Phys. **66**, 899 (1994)

[63] D. Sánchez-Portal, I. Souza and R. M. Martin, *Fundamental Physics of Ferroelectrics*, Ed. by R. Cohen, AIP Conference Proceedings, American Institute of Physics (Melville, 2000) vol. 535, pg. 111

[64] G. Saghi-Szabo, R. E. Cohen and H. Krakauer, Phys. Rev. Lett. **80**, 4321 (1998)

[65] D. Vanderbilt, J. Phys. Chem. Solids **61**, 147 (2000)

[66] M. Brandbyge, K. Stokbro, J. Taylor, J. L. Mozos and P. Ordejón, Mat. Res. Soc. Symp. Proc. **636**, D9.25.1 (2001)

[67] E. N. Economou, *Green's Functions in Quantum Physics*, Springer-Verlag (Berlin, 1983)

[68] A. J. Read and R. J. Needs, Phys. Rev. B **44**, 13071 (1991)

[69] E. K. U. Gross, C. A. Ullrich and U. J. Gossmann, in *Density Functional Theory*, Ed. by E. K. U. Gross and R. M. Dreizler, Plenum Press (New York, 1995), pg 149

[70] E. K. U. Gross, J. F. Dobson and M. Petersilka, in *Density Functional Theory II: Relativistic and Time Dependent Extensions*, Ed. by R. F. Nalewajski, Springer-Verlag (Berlin-Heidelberg, 1996), vol. 181, pg. 81

[71] K. Yabana and G. F. Bertsch, Phys. Rev. B **54**. 4484 (1996)

[72] A. Tsolakidis, D. Sánchez-Portal and R. M. Martin, cond-mat/0109488

[73] R. D. King-Smith, and D. Vanderbilt, Phys. Rev. B **49**, 5828 (1994)

[74] R. Cohen and H. Krakauer, Ferroelectrics **136**, 65 (1992)

[75] R. E. Cohen, and H. Krakauer, Phys. Rev. B. **42**, 6416 (1990)

[76] D. J. Singh, *Planewaves, Pseudopotentials, and the LAPW Method*, Kluwer Academic (Boston, 1994)

[77] P. Blaha, K. Schwarz, and J. Luitz, *WIEN97*, Vienna University of Technology, 1997. Improved and updated version of the original copyrighted WIEN code, published by P. Blaha, K. Schwarz, P. Sorantin, and S. B. Trickey, Comput. Phys. Commun. **59**, 399 (1990)

[78] J. Harada, T. Pedersen and Z. Barnea, Acta. Cryst. A **26**, 336 (1970)

[79] Ph. Ghosez, PhD Thesis; Ph. Ghosez, E. Cockayne, U. V. Waghmare and K. M. Rabe, Phys. Rev. B **60**, 836 (1999)

[80] Ph. Ghosez, X. Gonze, Ph. Lambin and J.-P. Michenaud, Phys. Rev. B **51**, 6765 (1995)

[81] Z. Zhong, R. D. King-Smith and D. Vanderbilt, Phys. Rev. Lett. **72**, 3618 (1994)

[82] P. Ordejón, E. Artacho, R. Cachau, J. Gale, A. García, J. Junquera, J. Kohanoff, M. Machado, D. Sánchez-Portal, J. M. Soler and R. Weht, Mat. Res. Soc. Symp. Proc. vol 677, pg. AA9.6.1 (2001)

[83] A. D. Becke, J. Chem. Phys. **98**, 1372 (1993)

[84] M. J. S. Dewar, E. G. Zoebisch and E. F. Healy, J. Amer. Chem. Soc. **107**, 3902 (1985)

[85] Gaussian 98 (Revision A.7), M. J. Frisch, G. W. Trucks, H. B. Schlegel, G. E. Scuseria, M. A. Robb, J. R. Cheeseman, V. G. Zakrzewski, J. A. Montgomery, Jr., R. E. Stratmann, J. C. Burant, S. Dapprich, J. M. Millam, A. D. Daniels, K. N. Kudin, M. C. Strain, O. Farkas, J. Tomasi, V. Barone, M. Cossi, R. Cammi, B. Mennucci, C. Pomelli, C. Adamo, S. Clifford, J. Ochterski, G. A. Petersson, P. Y. Ayala, Q. Cui, K. Morokuma, D. K. Malick, A. D. Rabuck, K. Raghavachari, J. B. Foresman, J. Cioslowski, J. V. Ortiz, A. G. Baboul, B. B. Stefanov, G. Liu, A. Liashenko, P. Piskorz, I. Komaromi, R. Gomperts, R. L. Martin, D. J. Fox, T. Keith, M. A. Al-Laham, C. Y. Peng, A. Nanayakkara, C. Gonzalez, M. Challacombe, P. M. W. Gill, B. G. Johnson, W. Chen, M. W. Wong, J. L. Andres, M. Head-Gordon, E. S. Replogle and J. A. Pople, Gaussian, Inc., Pittsburgh PA, 1998

[86] M. Machado, P. Ordejón, D. Sánchez-Portal, E. Artacho and J. M. Soler, physics/9908022

[87] J. Sponer, J. Leszczynski and P. Hobza, J. Phys. Chem. **100**, 1965 (1996)